

AD-A187 648

UNDERSTANDING THE HIP (HOT ISOSTATIC PRESSING)  
CONSOLIDATION OF P/M NICKE. (U) HENRY KRUMB SCHOOL OF  
MINES NEW YORK CENTER FOR STRATEGIC MAT J K TIEN

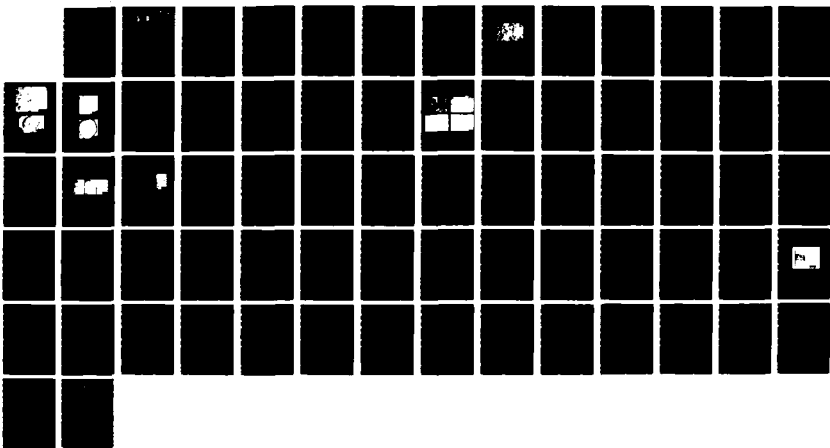
1/1

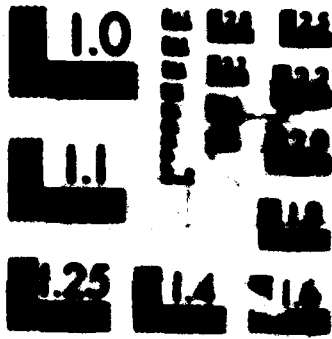
UNCLASSIFIED

NOV 87 AFOSR-TR-87-1893 AFOSR-82-0352

F/G 11/6 2

NL





MICROCOPY RESOLUTION TEST CHART  
NATIONAL BUREAU OF STANDARDS-1963-A

4. PERFORMING ORGANIZATION REPORT NUMBER(S) N/A			5. MONITORING ORGANIZATION REPORT NUMBER(S) N/A <b>AFOSR-TR. 87-1893</b>		
6a. NAME OF PERFORMING ORGANIZATION Columbia University-New York		6b. OFFICE SYMBOL (if applicable) N/A	7a. NAME OF MONITORING ORGANIZATION AFOSR/NE		
6c. ADDRESS (City, State and ZIP Code) Columbia University in the City of New York Box 20, Low Memorial Library, NY NY 10027			7b. ADDRESS (City, State and ZIP Code) Bldg 410 Bolling Air Force Base, DC 20332-6448		
8a. NAME OF FUNDING/SPONSORING ORGANIZATION Same as 7A		8b. OFFICE SYMBOL (if applicable) NE	9. PROCUREMENT INSTRUMENT IDENTIFICATION NUMBER AFOSR-82-0352		
8c. ADDRESS (City, State and ZIP Code) Same as 7B			10. SOURCE OF FUNDING NOS.		
			PROGRAM ELEMENT NO.	PROJECT NO.	TASK NO.
			61102F	2306	A1
11. TITLE (Include Security Classification) Understanding the HIP Consolidation of P/M Nickel-Base Superalloys					
12. PERSONAL AUTHOR(S) John K. Tien					
13a. TYPE OF REPORT FINAL		13b. TIME COVERED FROM 10-1-82 TO 9-31-87		14. DATE OF REPORT (Yr., Mo., Day) 11-87	15. PAGE COUNT 66
16. SUPPLEMENTARY NOTATION					
17. COSAT CODES			18. SUBJECT TERMS (Continue on reverse if necessary and identify by block number)		
FIELD	GROUP	SUB. GR.			
19. ABSTRACT (Continue on reverse if necessary and identify by block number) Powder metallurgy is a route often taken in superalloy processing, and hot isostatic pressing (P) is near-net shape is the most cost-effective method of superalloy powder consolidation. However, as HIP superalloys have been plagued by poor mechanical properties, which can be ascribed to materials cleanliness and to prior particle powder boundaries (PPB). The solution to the first problem is the policing of the process, and the solution to the second problem is more technical and pivots about altering the deformation mechanism comprising HIP densification to minimize PPB.					
20. DISTRIBUTION/AVAILABILITY OF ABSTRACT UNCLASSIFIED/UNLIMITED <input checked="" type="checkbox"/> SAME AS RPT <input type="checkbox"/> DTIC USERS <input type="checkbox"/>			21. ABSTRACT SECURITY CLASSIFICATION UNCLASSIFIED		
22a. NAME OF RESPONSIBLE INDIVIDUAL DR Alan H. Rosenstein			22b. TELEPHONE NUMBER (Include Area Code) (202) 767-4933	22c. OFFICE SYMBOL NE	

07 12 29 005

**FINAL TECHNICAL REPORT**

for

**AIR FORCE OFFICE OF SCIENTIFIC RESEARCH  
Grant AFOSR-82-0352**

**"Understanding the HIP Consolidation  
of P/M Nickel-Base Superalloys"**

**Monitor: Alan H. Rosenstein  
Principal Investigator: John K. Tien  
Period: 1 October 1982 - 31 September 1987**

**Center for Strategic Materials  
Henry Krumb School of Mines  
Columbia University  
November 1987**

Accession For	
NTIS CRA&I	<input checked="" type="checkbox"/>
DTIC TAB	<input type="checkbox"/>
Unannounced	<input type="checkbox"/>
Justification	<input type="checkbox"/>
By _____	
Distribution / _____	
Availability Codes	
Dist	Avail and/or Special
<b>A-1</b>	



## Table of Contents

I. Executive Abstract	page 1
II. Progress Report for Entire Project Period	5
A. Chronology of Task Completion	5
B. Powder Characterization	6
C. Material Characterization	12
D. Experimental HIP and CAP Runs	22
E. Superalloy HIP Modeling	30
F. Variable Pressure HIP Runs	49
G. Superconductor HIP Modeling	52
H. Composite HIP Modeling	61
III. Theses from this Research	63
IV. Publications and Presentations from this Research	64

## I. Executive Abstract

Powder metallurgy is a route often taken in superalloy processing, and hot isostatic pressing (HIP) to near-net shape is the most cost-effective method of superalloy powder consolidation. However, as-HIP superalloys have been plagued by poor mechanical properties, which can be ascribed to materials cleanliness and to prior particle powder boundaries (PPB). The solution to the first problem is the policing of the process, and the solution to the second problem is more technical and pivots about altering the deformation mechanism comprising HIP densification to minimize PPB.

Previously the mechanisms of densification during HIP have not been well understood. It had been thought that, under the commercial temperature and pressure conditions of HIP of superalloy powders, deformation occurred primarily by creep. Since the commercial powder consists of particles of unequal size, a variation in the extent of deformation is seen. The small particles are smeared in between the large particles, which remain relatively undeformed (Figure 1). The undeformed boundaries or PPB are sites for precipitation of blocky gamma prime and deleterious carbides. If deformation of all powder particles could be maximized, PPB would be minimized and a more reliable consolidate would be the result. However, the knowledge of mechanisms and kinetics of HIP was previously insufficient to indicate temperature and pressure conditions for uniform maximum deformation of all powder particles.

This research program was undertaken to advance the scientific understanding of HIP and to apply that understanding to HIP processing and demonstrate improved material. In this five year program, the goals set in previous proposals have been met.

In Year One, the argon-atomized Rene 95 powder used in the HIP studies was completely characterized in terms of surface morphology, porosity,

microstructure, and carbon and carbide content. In Years One and Two, HIP runs were done at one commercial pressure and temperature (1120°C and 103 MPa) for varying hold times (5-180 minutes) and for three different size distribution of powders: monosized (-170 +200), bimodal (80% -170 +200 20% -400 +500), and full size (-150 mesh). Contrary to industrial belief, densification was nearly instantaneous. Full density was reached even with a hold time of only 5 minutes. The mechanism of deformation at these conditions is mainly athermal plastic flow rather than creep deformation. It was found that the rapid deformation and/or full size powder distribution led to a greater density of PPB.

Concurrently, consolidation at atmospheric pressure (CAP) runs were also conducted at two temperatures (1218°C and 1121°C, at 0.101 MPa) for varying hold times for the full powder size distribution, and experimental densification rate laws have been obtained. At the higher temperature of 1218°C, sintering and grain coarsening are dominant, since the  $\gamma'$  solvus of Rene 95 is around 1160°C and the solidus is around 1246°C.

In Years Two and Three, in order to promote more uniform densification deformation, i.e., creep, additional HIP runs were done at two conditions of lower pressures and temperatures (900°C, 103 MPa and 1000°C, 10.3 MPa) for varying hold times (5-180 minutes) and for the same three powder size distributions. Experimental densification rate laws have been obtained. No fully dense material was obtained, even after 3 hours hold time. The uniformity of densification was analyzed by examination of PPB morphology.

In the second and third years, high temperature tensile tests were run on as-HIP Rene 95 to determine the strain rate and temperature regime of superplastic deformation. In addition, stepped strain rate tensile tests have been performed to examine the path-dependence of deformation.

In pace with the experimental work, an analytical model for the mechanisms

and kinetics of HIP densification was developed. In the fourth year, the HIP modeling was used to predict variable pressure HIP runs which would maximize densification by a single mechanism and promote uniform deformation. In the final year, the model has been extended to include other material systems such as composites and oxide superconductors.

This research has resulted in 15 publications so far, 16 presentations and 9 theses (including 2 doctoral theses).

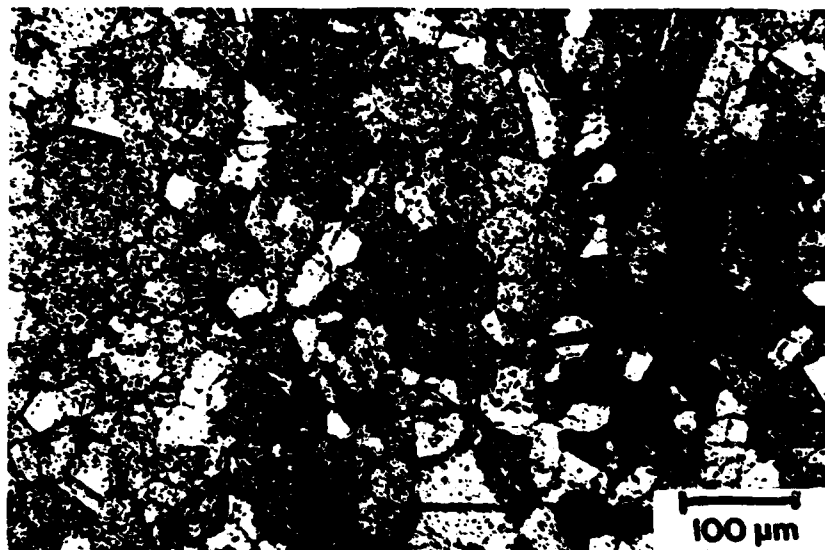
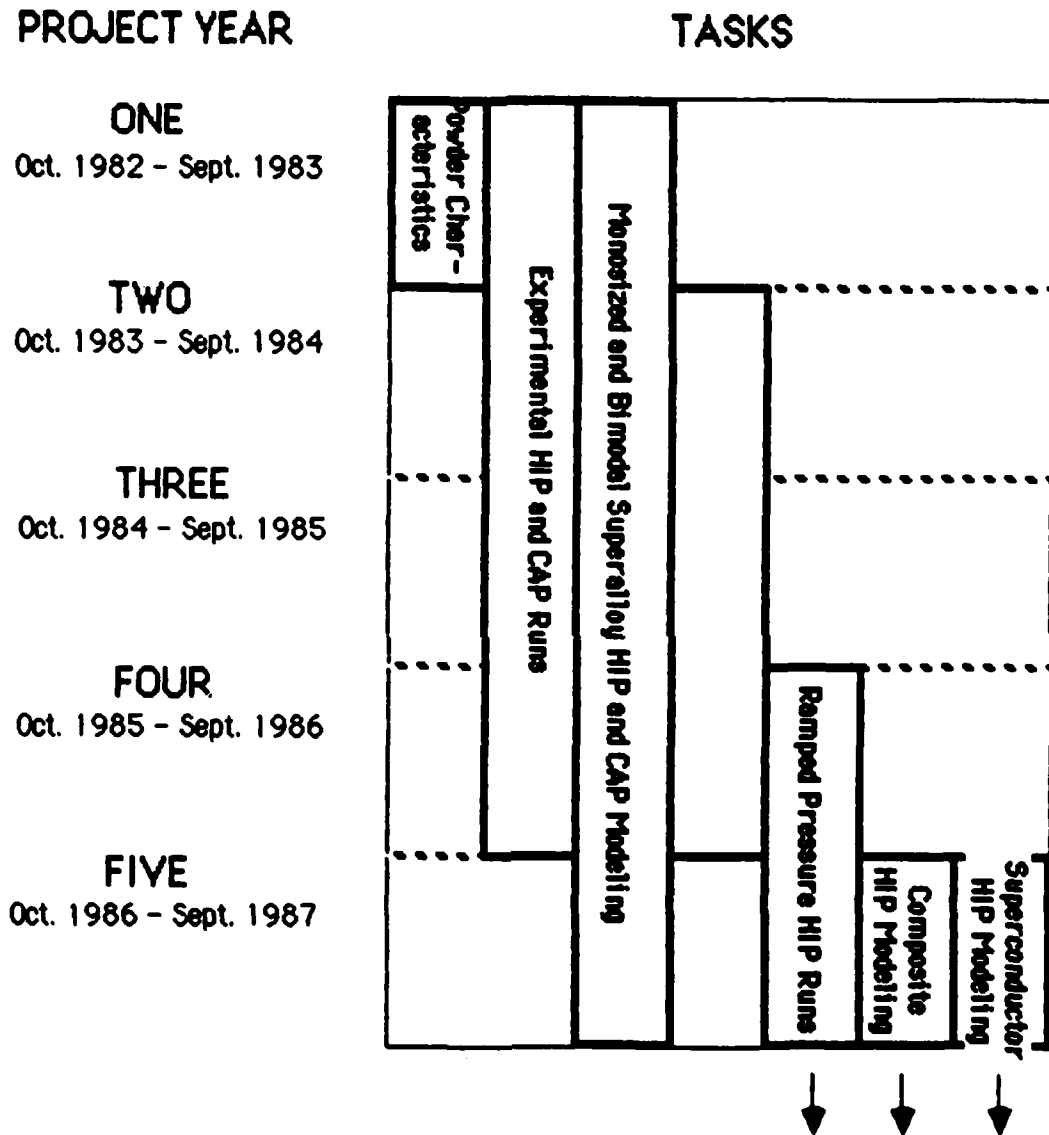


**Figure 1.** Rene 95, commercial powder distribution and HIP conditions.

II. Progress Report for Entire Project Period

A. Chronology of Task Completion



## B. Powder Characterization

The nominal composition of Rene 95 is given in Table I. The powders were produced by the Argon Atomization (AA) process. The carbon level of the powders and the HIP consolidated material was 0.049 wt.%. Approximately 33% of the AA powder was -170 mesh ( $<90 \mu\text{m}$ ) with the peak of the distribution between -400 + 500 mesh (33-38  $\mu\text{m}$ ). This constitutes the normal distribution. The monosized particles are approximately 85  $\mu\text{m}$  in diameter (screened to a narrow size range -170 + 200 mesh, i.e., 75-90  $\mu\text{m}$  powder). The bimodal size particles were screened to -170 + 200 mesh (75-90  $\mu\text{m}$ ) and -450 to +500 mesh (33- 38  $\mu\text{m}$ ) and combined in weight percents of 80 and 20% respectively. An actual powder size distribution is given in Table II.

Relevant to the nature and rate of HIP densification is the powder particle shape and size (morphology), porosity within the particle itself, and the particle microstructure, that is, whether microcrystalline or dendritic. Since the prior particle boundary problem is caused by precipitation of carbide films, it is also necessary to determine the dissolved carbon content in the particles. The results of these investigations are provided below.

Surface Morphology: The particles are generally spherical with many of the particles exhibiting multiple solidification initiation sites ('starbursts'). Some 'satellite' structures are also evident, i.e., fine particles welded to coarse particles, see Figure 2. The particles are occasionally enveloped in metal shells, which occur when a liquid droplet impinges on and surrounds an already solidified particle.

Porosity: The percent of particles with central pores (see Figure 2) for various

particle diameters is given in Table III. Thus, except for small particle sizes (<10  $\mu\text{m}$ ), the % volume occupied as enclosed porosity appears to be significant. Table IV shows how interdendritic shrinkage voids are distributed as the particle diameter varies. It needs to be determined how the enclosed porosity affects the densification kinetics and the mechanisms of deformation responsible for the densification.

Sectioned Particle Microstructures: As indicated in Table V, the particles are essentially dendritic for the larger particle sizes with the microcrystalline and cellular structures more probable at smaller particle size ranges, see Figure 2.

Dissolved Carbon and Carbide Content: MC type Nb-rich carbide was extracted by digesting the powder specimens with 10 vol. % bromine methanol. Carbon analyses were performed on the residues to determine wt.% of alloy carbon fixed as MC, and the remainder of the carbon was assumed to be dissolved. In this work dissolved carbon was found to stay at about 20% for close sieve fractions down to 150  $\mu\text{m}$ , below which it increased. X-ray diffraction showed no crystalline phases other than MC in the residues. Thus, the tendency for carbide precipitation during HIP can be expected to increase as particle size decreases. On the other hand, the extent of deformation also increases for the smaller particles, so that PPB effects can be seen to be a trade-off between the two opposing tendencies.

Experimental Preparation: The powders were filled into stainless steel HIP cans, ranging from 10 to 18 cm in height and 4 to 15 cm in diameter. All cans were degassed and sealed by welding.

**Table I.** Nominal Composition of Rene 95, weight percent.

<b>C</b>	<b>B</b>	<b>NI</b>	<b>Al</b>	<b>Ti</b>	<b>Cr</b>	<b>Co</b>	<b>Mo</b>	<b>W</b>	<b>Zr</b>	<b>Nb</b>
0.06	0.01	bal	3.5	2.5	13.0	8.0	3.5	3.5	0.05	3.5

**Table II.** Distribution of Powder.

	<b>Full</b>	<b>Bimodal</b>	<b>Monosized</b>
<b>Tap Density</b>	63%	61%	58%
<b>Sieve Size</b>			
-140 +170	0.6	1.9	3.0
-170 +200	4.3	61.9	70.4
-200 +230	4.7	19.9	26.6
-230 +270	10.0	0	0
-270 +325	6.4	0	0
-325 +400	14.8	0.7	0
-400 +500	35.9	14.3	0
-500	23.3	1.3	0

**Table III.** Internal Porosity in Powders.

<b>Particle Diameter,</b> <b>µm</b>	<b>Percent of Particles</b> <b>with Central Pores</b>
215	65
170	67
125	44
100	45
65	14
35	5

**Table IV.** Distribution of Interdendritic Shrinkage Voids.

<b>Particle Diameter,</b> <b>μm</b>	<b>Distribution</b>
200 - 230	throughout particles
97 - 104	near surfaces
33 - 38	none observed

**Table V.** Cooling Microstructures.

<b>Particle Diameter,</b> <b>μm</b>	<b>Dendritic</b> <b>%</b>	<b>Cellular</b> <b>%</b>	<b>Microcrystalline</b> <b>%</b>
107	100	0	0
38	95	5	0
12	90	9	1

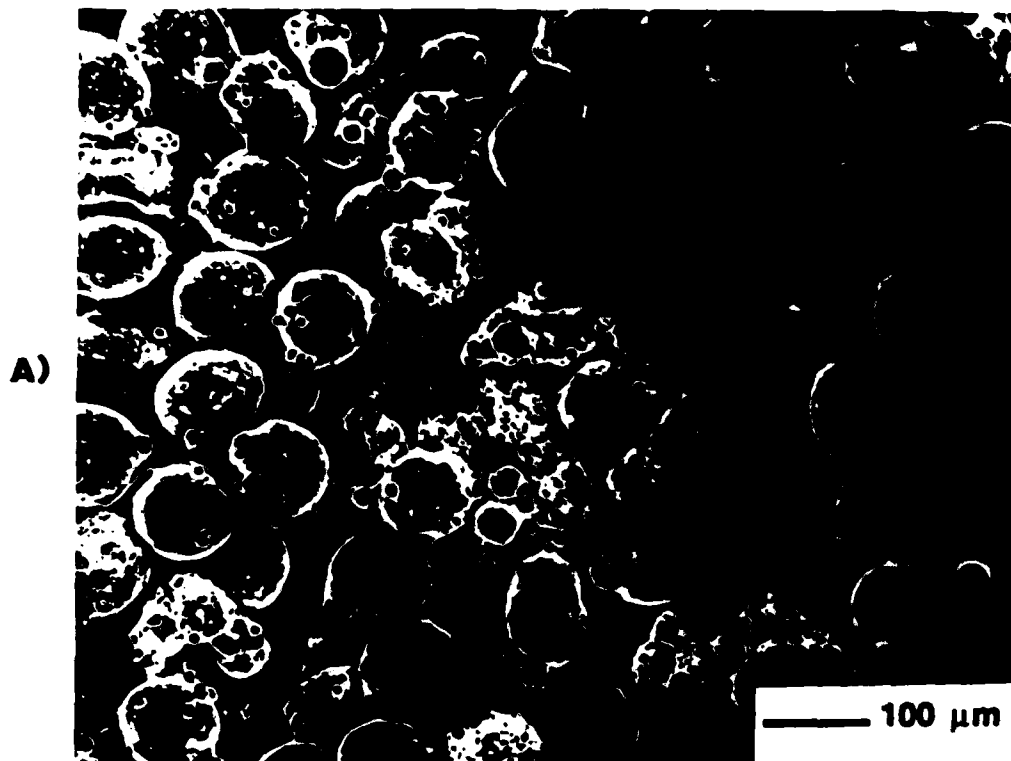
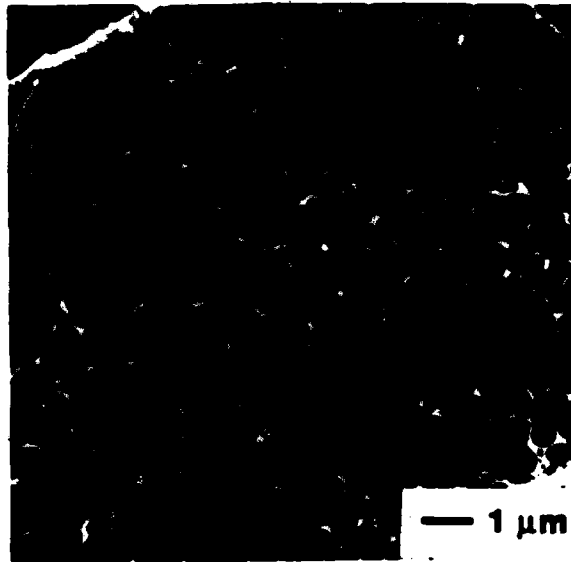
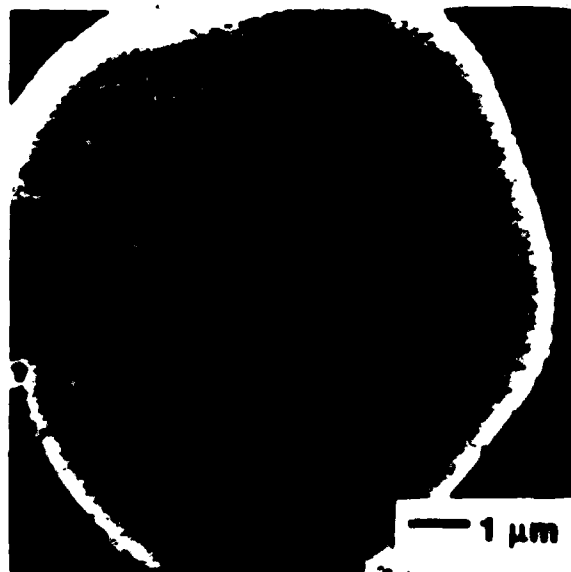


**Figure 2.** Argon atomized powder a) loose and in cross section exhibiting b) dendritic structure, a central enclosed pore within a powder particle and "satellite" particles; c) microcrystalline structure and d) cellular structure.

**C)**



**D)**



C. Material Characterization: Regimes in Pressure and Temperature of the  
Various Deformation Mechanisms

The mechanisms of deformation in various pressure/temperature regimes were determined for use as input into the HIP models. True strain rate controlled tensile tests were run at strain rates ranging from  $2 \times 10^{-5}$ /sec to  $1 \times 10^{-2}$ /sec and temperatures of 1000°, 1050°, 1100°, and 1150°C, temperatures in the range where HIP and forging of Rene 95 is done. The strain rate results are indicated in Figure 3 as a log-log plot of the flow stress ( $\sigma$ ) versus strain rate ( $\dot{\epsilon}$ ). The slope of the curves, that is, the strain rate exponent ( $m$ ), is plotted in Figure 4 as a function of the strain rate and shows an anticipated peak in the exponent  $m$  at the temperatures investigated. The ductility results are shown in Table VI with the associated values of  $m$ .

Superplasticity is expected to dominate the deformation behavior at the peak ( $m > .3$ ) although relatively large ductilities (indicating some superplastic behavior) was obtained even at off-peak values of  $m$  ( $m < .2$ ), i.e., at 1150°C and  $1 \times 10^{-4}$ /sec,  $m = .19$  although the ductility was 148 percent. This appears to be due to grain coarsening (Figure 5), especially since 1150°C is above the  $\gamma'$  solvus. We also found evidence of low ductility (40 percent) at close to peak value of  $m$  at the temperature of 1100°C, and we believe that prior particle boundaries may inhibit superplastic deformation by offering sites for crack nucleation especially at the higher stress regimes and higher strain rates. Thus optimal superplastic behavior in terms of ductility appears to be obtained at lower temperatures and when the peak value of  $m$  is reached at lower strain rates.

To further elucidate the deformation mechanisms, the activation energy ( $Q$ ) for the deformation at various values of stress was found and the results of  $Q$

versus  $\sigma$  are shown in Figure 6 along with literature values of  $Q$  for various mechanisms for the purposes of comparison. Consistent with our analysis, superplastic behavior appears to be favored at intermediate stresses. If the stresses are too low, diffusion is favored whereas at high stresses a transition appears to occur to a power law creep mode. We believe that the regime of superplastic behavior can be further extended by limiting PPB formation, particularly for the lower temperature HIP runs for which the creep stresses are relatively high.

In order to more fully investigate the superplastic behavior of Rene 95, stepped strain rate tension tests (Figure 7) were used (initially only to conserve material). However we found that the flow stress of the material was path dependent on the strain rates at the temperature investigated, and  $n$  could not be validly determined (Figure 8). Further investigation into this effect showed that another aerospace material, Ti-17, was indeed strain rate path independent at temperatures typically used for forging of the material, for stepped strain rate tests in compression (Figure 9). The titanium alloy is probably path independent due to the lack of work hardening, as can be seen in the very flat  $\sigma$ - $\epsilon$  curve at these temperatures, particularly since the forging temperature for Ti-17 is relatively high compared to the melting temperature of the material. Rene 95 is isothermally forged below the  $\gamma'$  solvus temperature to prevent excessive grain growth, and the material undergoes work hardening. These results have some impact in forging as well as in HIP, because tensile and compression tests are used as input for predictive forging modeling, and for some cases, the forging process may not be accurately represented by single strain rate tensile or compression tests.

**Table VI. Ductility and m values.**

	$2 \times 10^{-5}$	m	$1 \times 10^{-4}$	m	$1 \times 10^{-3}$	m	$3 \times 10^{-3}$	m	$1 \times 10^{-2}$
1000°C	(240%) *	.46	(239%)						
1050°C	(234%) *	.45	(515%)	.49	(160%)	.40	(60%)		
1100°C	(190%) *	.22	(445%)	.38	(160%)	.46	(72%)	.35	(35%)
1150°C			(148%)	.16	(60%)	.37	(40%)	.33	(40%)

\* Test was terminated before failure.

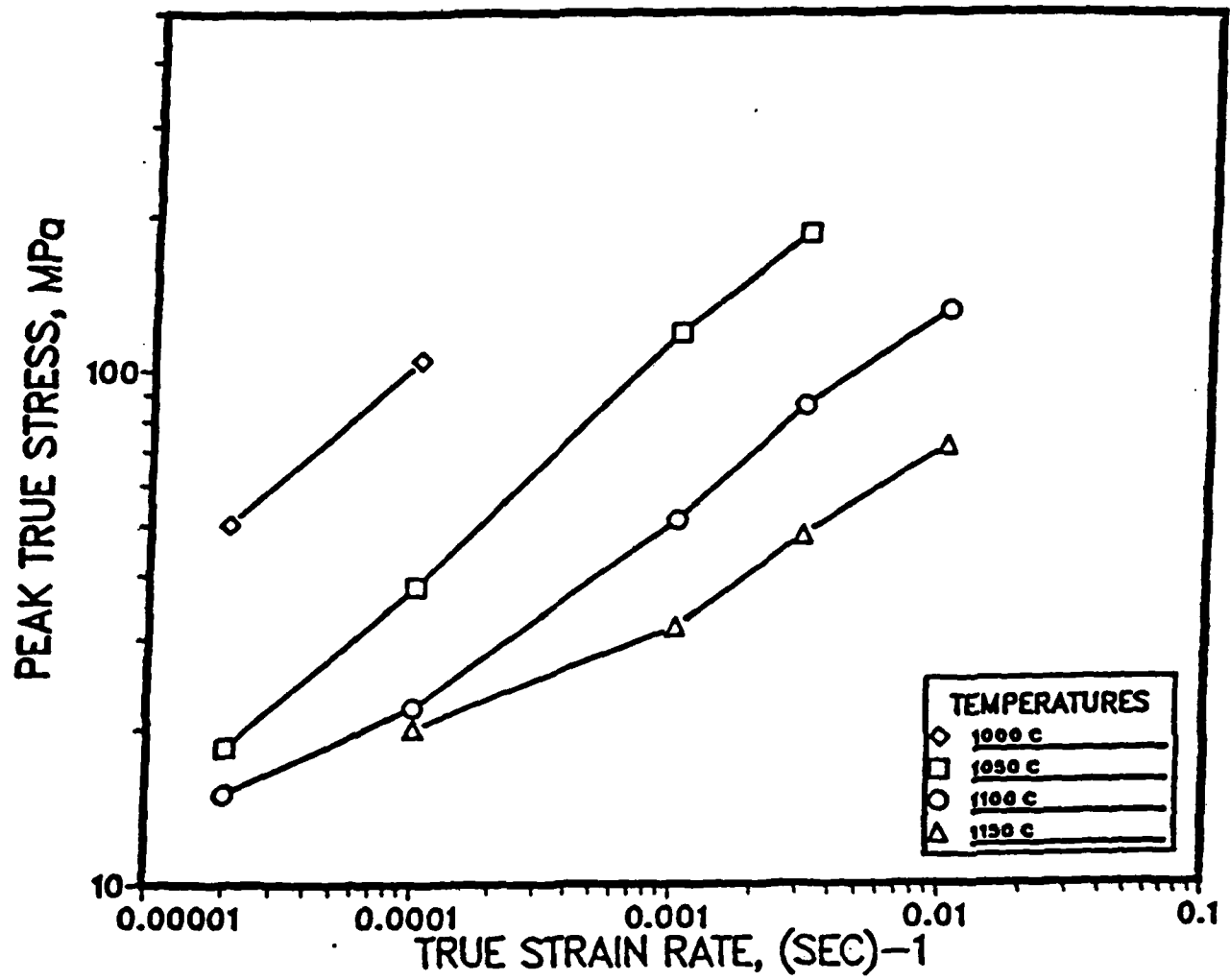
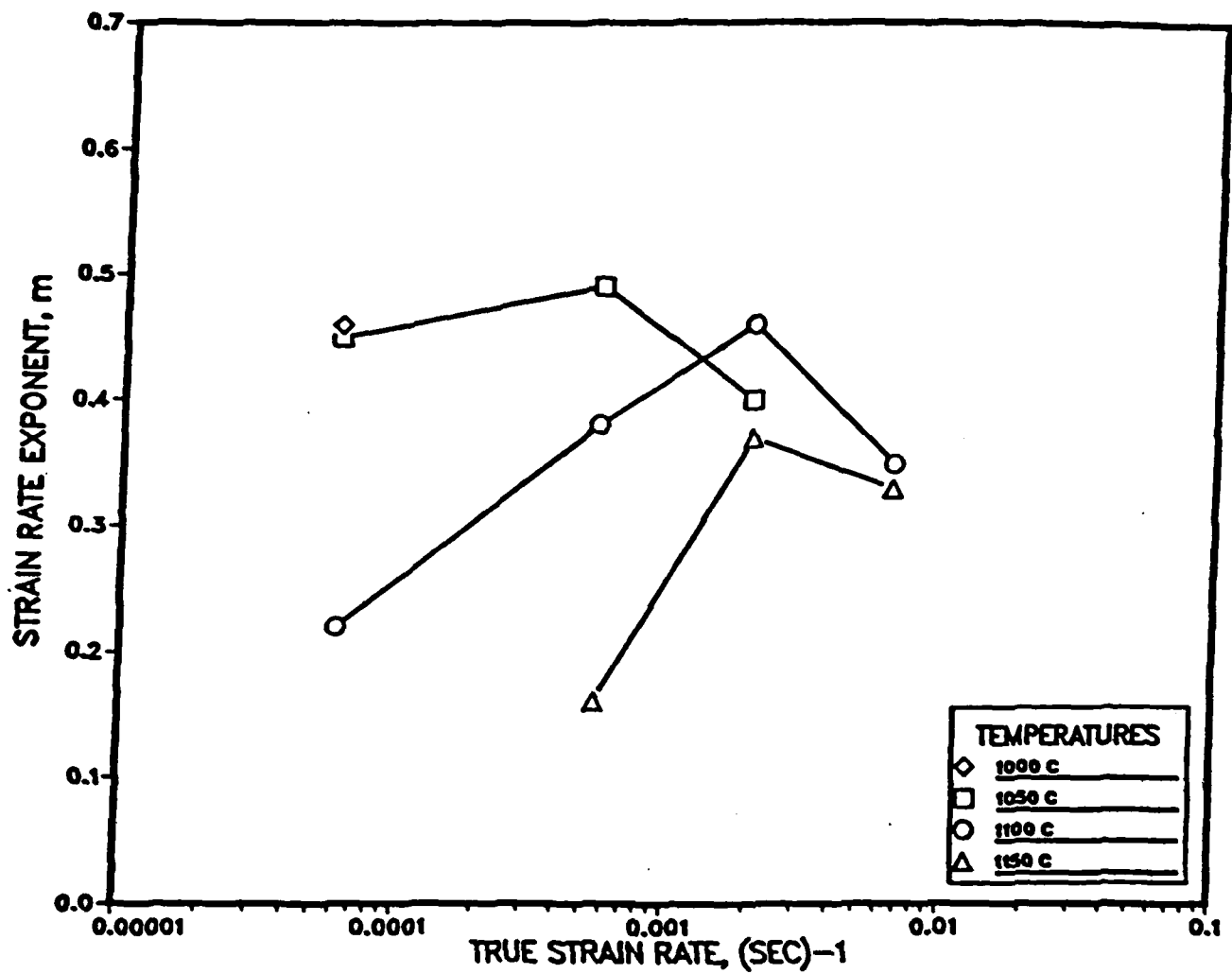


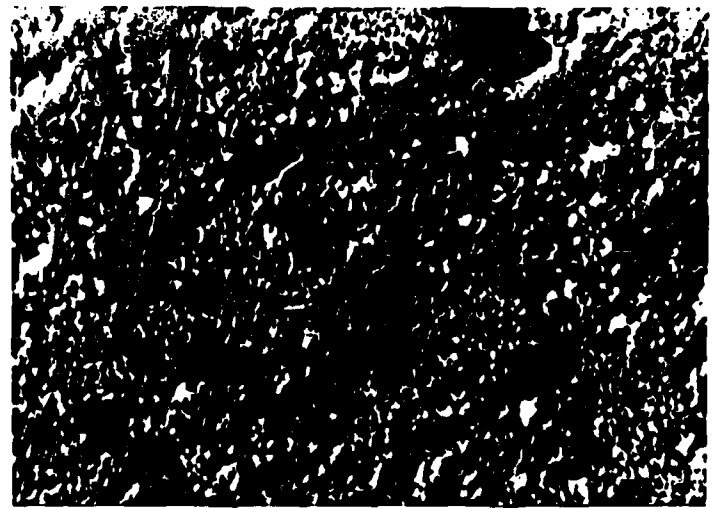
Figure 3. Peak true stress versus true strain rate, for Rene 95 at several temperatures.



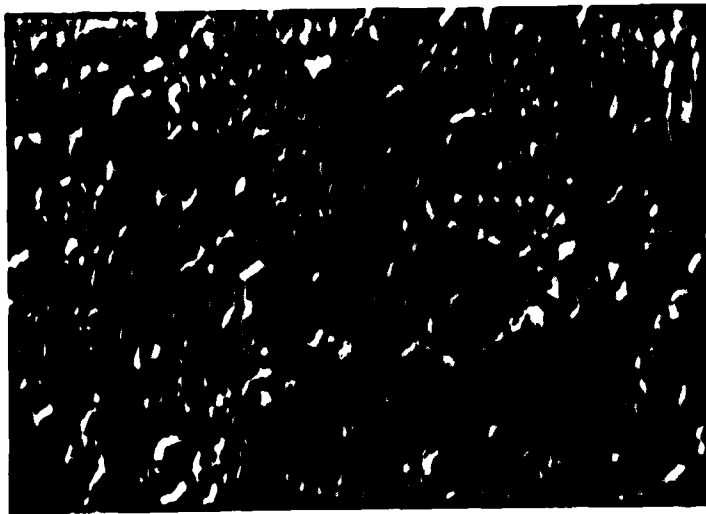
**Figure 4.** Strain rate exponent ( $m$ ) versus true strain rate for Rene 95 for several temperatures. Generally, superplastic behavior occurs at  $m > 0.3$ .



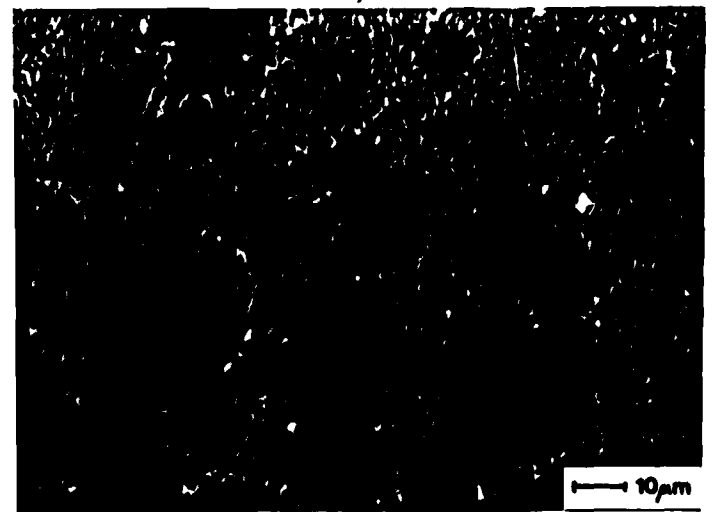
as-HIP



1050°C,  $1 \times 10^{-4}$



1100°C,  $2 \times 10^{-5}$



1150°C,  $1 \times 10^{-4}$

**Figure 5.** Rene 95 a) as-HIP and tested at b)  $1050^{\circ}\text{C}$ ,  $1 \times 10^{-4} \text{ sec}^{-1}$ , c)  $1100^{\circ}\text{C}$ ,  $2 \times 10^{-5} \text{ sec}^{-1}$  and d)  $1150^{\circ}\text{C}$ ,  $1 \times 10^{-4} \text{ sec}^{-1}$  showing coarsening and cavitation.

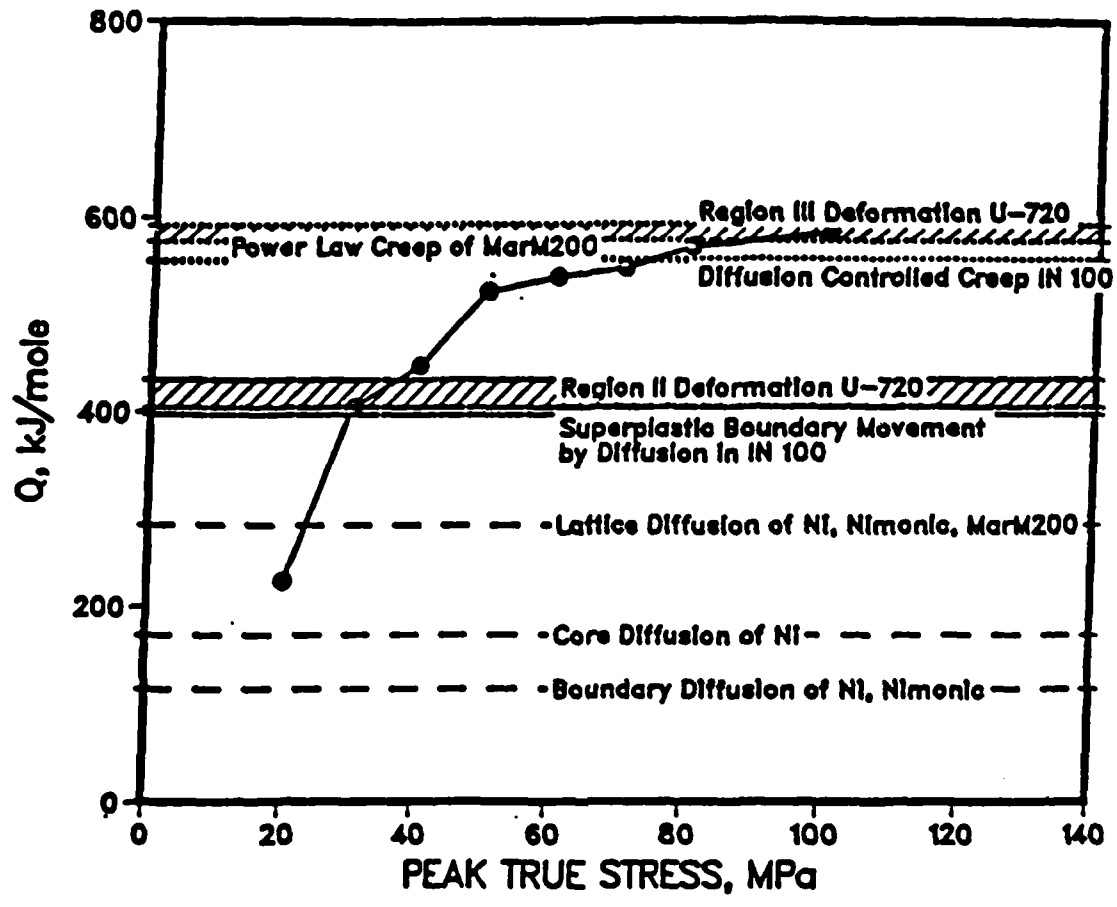


Figure 6. Activation energy versus peak true stress. Note the transition from diffusion to power law creep.

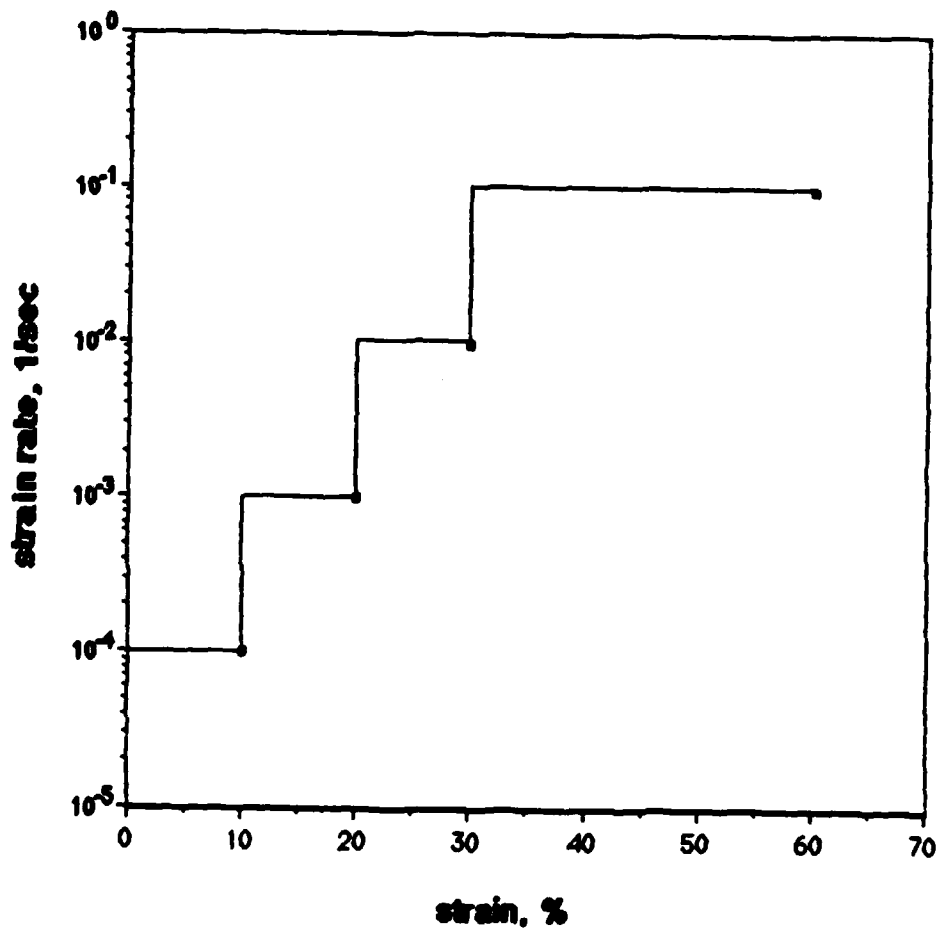
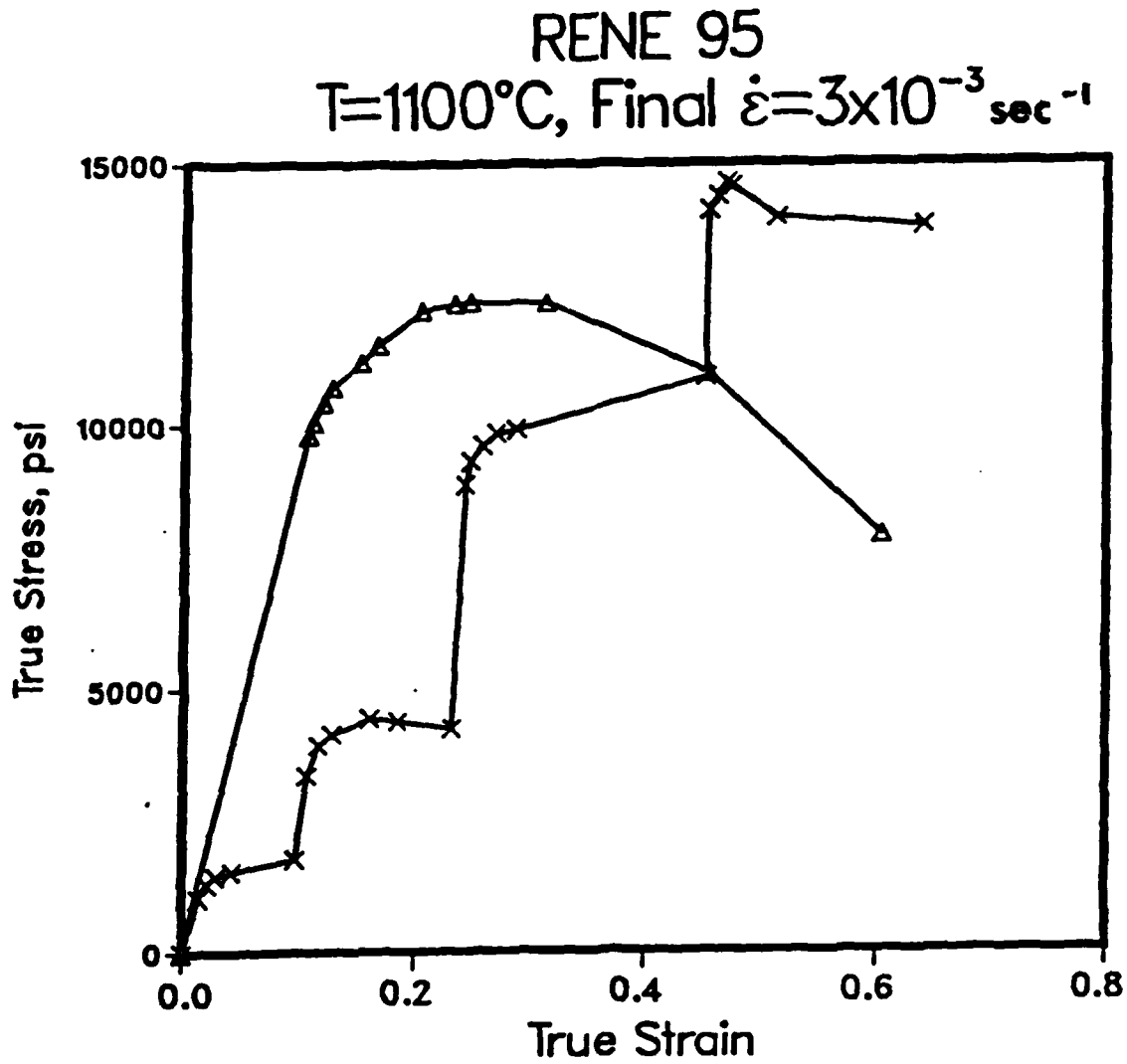
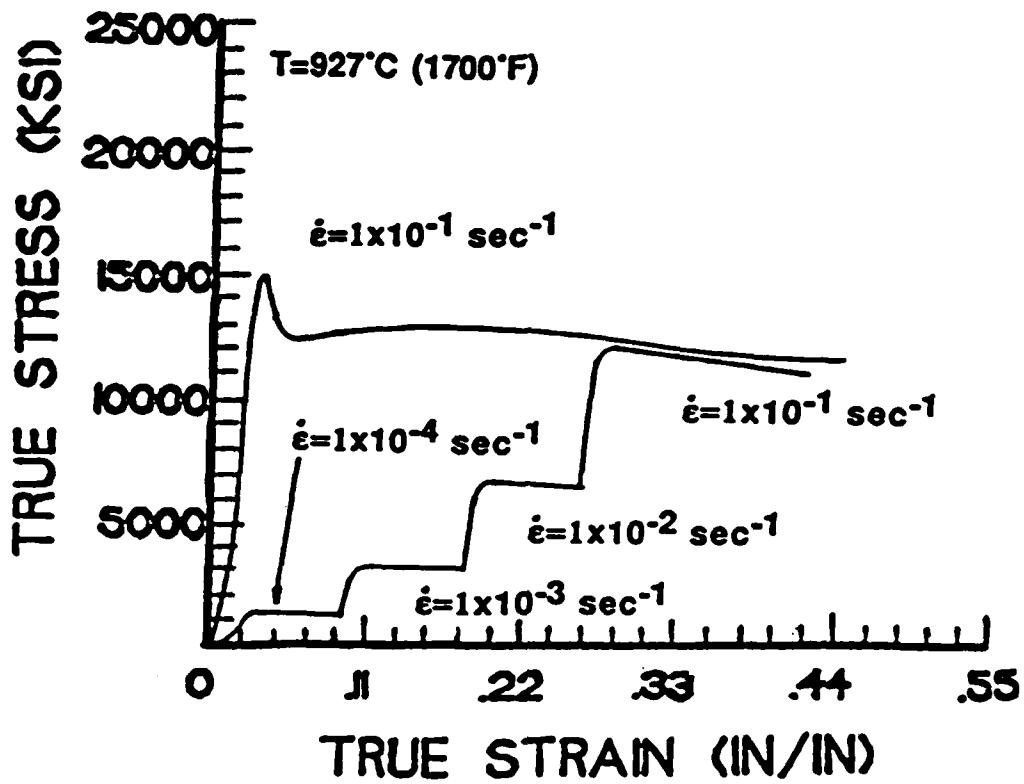


Figure 7. Schematic of a stepped strain rate test. There is a 10%  $\epsilon$  dwell at each strain rate.



**Figure 8.** Single and stepped strain rate tensile tests for Rene 95. Note the difference in flow stress for the same strain rate.



**Figure 9.** Single and stepped strain rate tensile tests for Ti-17. Note the agreement flow stress for the same strain rate.

#### D. Influence of Particle Size Distribution and HIP Conditions on HIP

##### Densification

The kinetics of powder densification and powder morphological changes were determined initially at one commercial pressure (P) and temperature (T) condition of 1120°C and 103 MPa for the nickel base superalloy Rene 95. The HIP cycle used included a one hour heatup and pressurize, a hold time and a one hour cooldown and depressurize. Densities were measured (volume was determined by water displacement). It was found (a surprising fact to the relevant industry) that consolidation for all the particle distribution cases occurred very rapidly (full density reached in 5 minutes, see Table VII), mainly by instantaneous plastic flow instead of by local creep deformation. It was also found that non-creep deformation and/or a full distribution of particle sizes can result in a greater number of undeformed particles in the consolidates. The boundaries of these undeformed particles can become prior particle boundaries (PPB). For example, see Figure 10 showing minimum PPB for the monosized case and maximum for the full size distribution.

At the lower pressure of 10.3 MPa, densification was somewhat less rapid (see Table VII), and there was clear evidence (see Figure 11) that the smaller particles underwent the greater proportion of plastic deformation during the HIPing process.

To obtain clear kinetic data, CAP (1 atmosphere, 0.101 MPa) densification on a full size distribution was conducted at two temperatures of 1218°C and 1121°C, and the densification results from these tests are shown in Table VIII. Clearly, the densification, as expected, is much slower under CAP pressure conditions than at the commercial pressure conditions.

In Years Two and Three, HIP densification was conducted at three lower

temperatures and pressures (800°C, 103 MPa; 900°C, 103 MPa and 1000°C, 10.3 MPa) for all three size distribution cases. The densification results (Table IX) indicate relatively slower densification as with CAP, and powder particles are probably undergoing creep and/or superplastic deformation.

Figures 12, 13 and 14 show the effect on kinetics of temperature, pressure, and powder size distribution, respectively. The vertical dotted line represents the four hour hold time, as is generally reported for HIP of Rene 95 in the literature. Lowering either the temperature or the pressure slows the densification rate, however temperature (at least at 103 MPa) has a greater influence on the kinetics. For only a 200°C drop in temperature, densification is slowed to the point that none of the HIP runs reached full density in four hours (Figure 12), but an order of magnitude drop in pressure still yields fully dense material within four hours (Figure 13). The powder size distribution appears to have only a small effect on kinetics, due mainly to the difference in initial powder densities. This effect lessens as densification progresses (see Figure 14).

**Table VII. Densities of First Year HIP Runs.**

Powder Distribution		T, °C	P, MPa	Relative Density, % (100% = 8.290 g/cm <sup>3</sup> )					
				Hold Times, min					
				5	15	30	60	120	180
Full		1121	103.0	100	100	-	100	-	100
Bimodal		1121	103.0	100	100	100	100	100	100
Monosized		1121	103.0	100	100	100	100	100	100
Full		1121	10.3	92.6	96.5	-	-	-	99.6

**Table VIII. Densities of CAP Runs.**

Powder Distribution		T, °C	P, MPa	Relative Density, % (100% = 8.290 g/cm <sup>3</sup> )					
				Hold Times, min					
				5	15	60	180	420	960
Full		1121	0.101	63.9	69.0	67.5	71.4	74.9	78.0
Full		1218	0.101	66.2	69.8	77.8	90.8	94.0	99.0

**Table IX. Densities of Second Year HIP Runs.**

Powder Distribution		T, °C	P, MPa	Relative Density, % (100% = 8.290 g/cm <sup>3</sup> )			
				Hold Times, min			
				5	15	60	180
Full		800	103.0	-	-	76.1	-
Bimodal		900	103.0	79.1	81.6	84.2	89.4
Monosized		1000	10.3	75.7	77.3	80.4	85.2
Full		1000	10.3	75.0	77.2	85.1	91.4
Monosized		1000	10.3	71.6	79.6	81.1	85.2

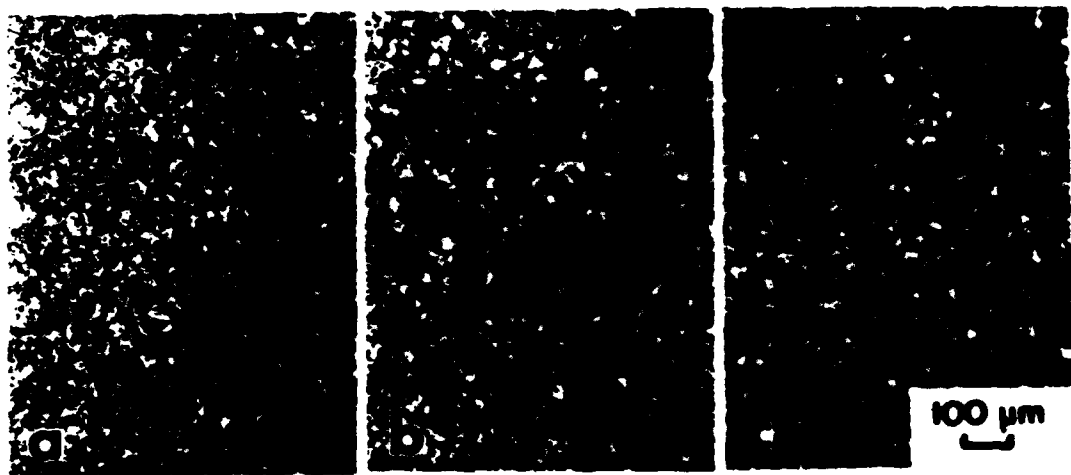


**Figure 10.** Optical micrographs of HIP Rene 95 powder after a five minute hold time at 1121°C and 103 MPa for a) monosized, b) bimodal and c) full-sized powder distributions.

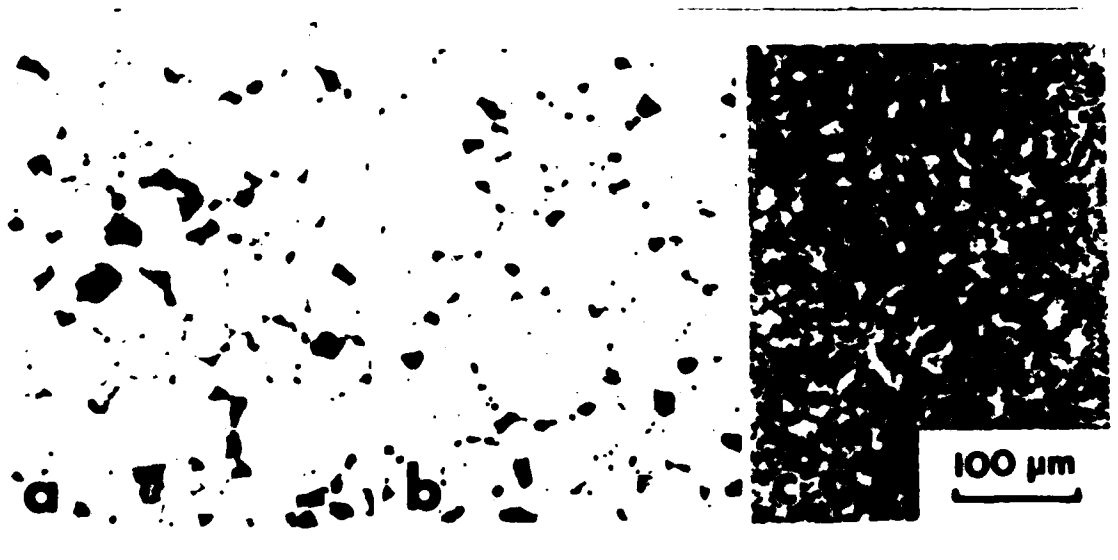


**Figure 11.** Optical micrographs of HIP Rene 95 powders (full size distribution) showing morphological changes of powders as a function of hold time at 1121°C and 10.3 MPa: a) 5 minutes, b) 15 minutes and c) 60 minutes.

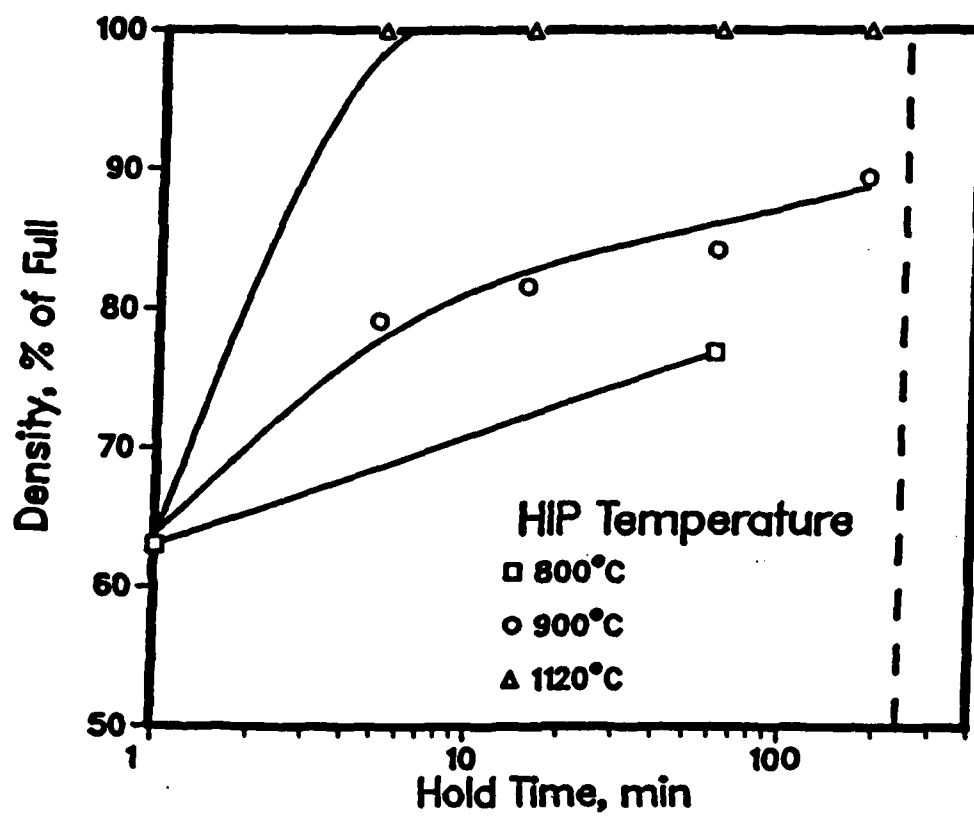


**Figure 12.** Effect of temperature on kinetics of full sized Rene 95 powder at 103 MPa.

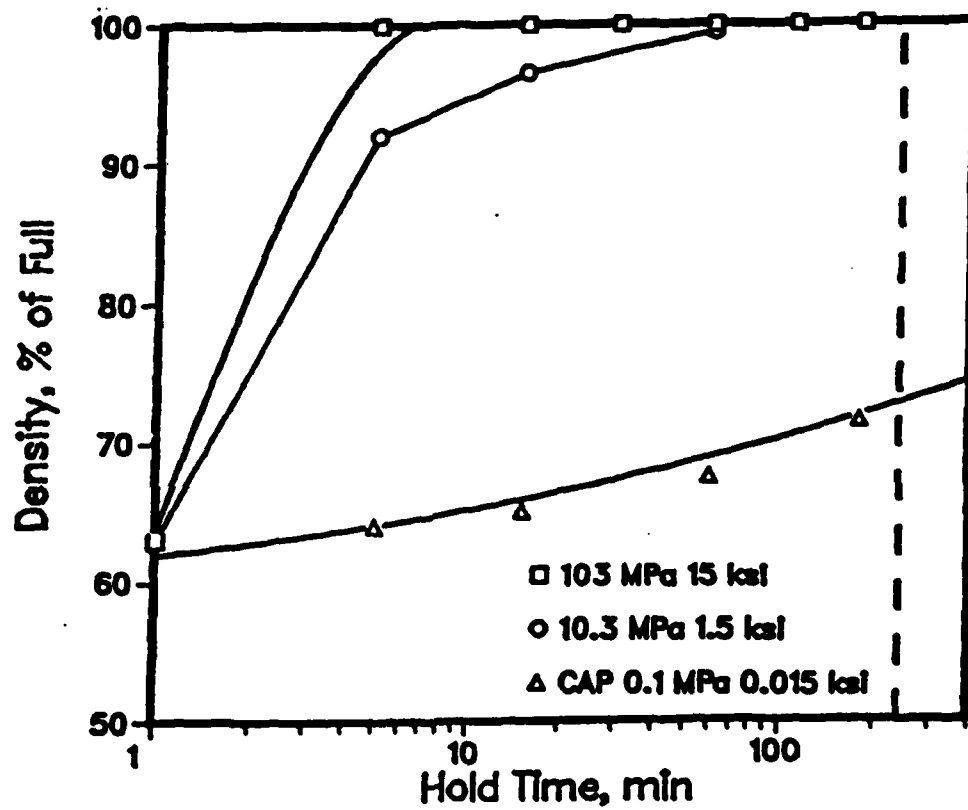


Figure 13. Effect of pressure on kinetics of full sized Rene 95 powder at 1121°C.

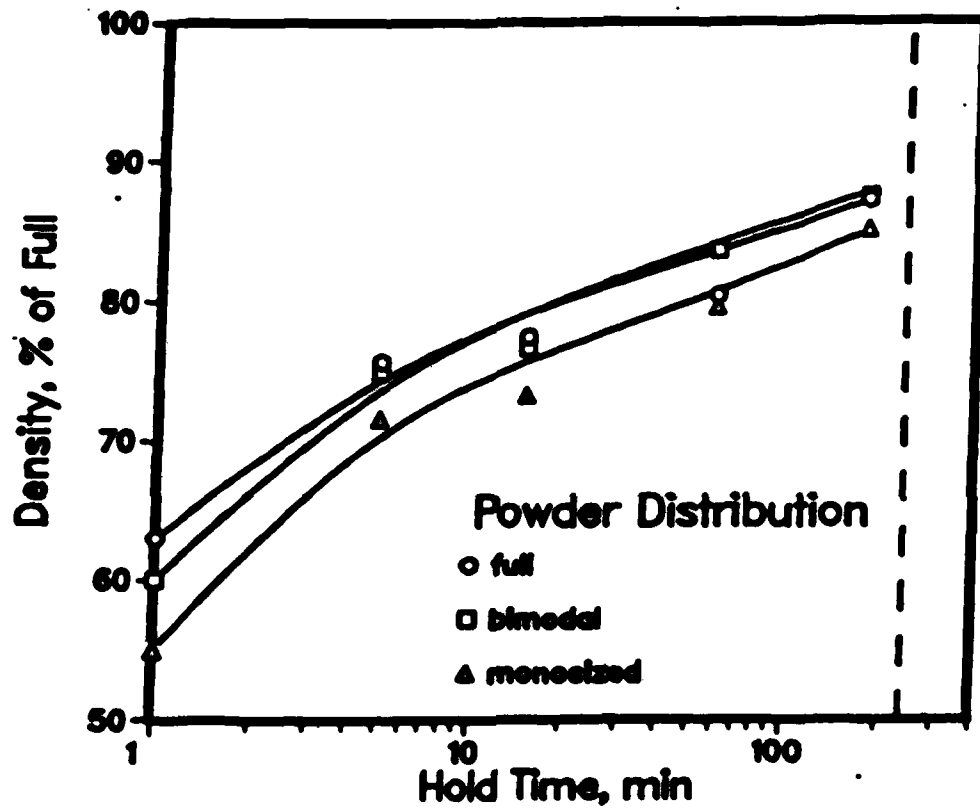


Figure 14. Effect of powder distribution on kinetics of Rene 95 powder at 1000°C and 10.3 MPa.

E. Analytical Model for HIP Densification

Previous modeling of densification kinetics by Arzt, Ashby, and Easterling considered only a single particle size. However, in reality P/M consolidates are made of a natural distribution of powder sizes below a given mesh size. The possible disparity between theory and practice prompted the development of a new model to incorporate the influence of a particle size distribution on both the kinetics of HIP densification and the deformation mechanisms operating during HIP consolidation of superalloy powders. This is done for a more realistic bimodal (or two size) distribution of powders. In order to rederive the HIP densification mechanism map for a bimodal particle distribution, expressions were derived for (a) the distribution of unequal sized particles in a random mixture, and (b) the relationship between the interparticle contact force and the applied pressure.

The radial distribution of powder particles in a bimodal distribution was also experimentally determined by point counting on sections of powder mounted in plastic. Figure 15 shows the results as  $(N_{ij})$ , the number of particles of size  $j$  around a particle of size  $i$ , as a function of radial distance normalized to the radius of the small particles ( $i, j = 1$ ). The large particles are denoted as  $i, j = 2$ .

The results of (a) are obtained in open form using the Percus-Yevik hard sphere approximation for the molecular structure of liquid alloys as derived by J.L. Lebowitz, namely,

$$r_{g_{ij}}(r) = \frac{\delta+1}{2\pi i} \int_{\delta-1}^{\delta+1} \frac{12(n_i n_j)}{i j} G(s) \exp(sr) ds \quad (1)$$

where  $g_{ij}(r)$  is the radial distribution function between the  $i^{\text{th}}$  and  $j^{\text{th}}$  particle,  $\eta_i = \pi\rho_i/6$  where  $\rho_i$  is the density of the  $i$ -type atom in nos./unit volume.  $G_{ij}$ , which is the number of atoms at any given distance,  $r$ , from a central atom and in a thin shell of thickness,  $dr$ , is given by

$$G_{ij}(r) = \rho_j 4\pi r^2 g_{ij}(r) dr \quad (2)$$

To relate the applied HIP pressure  $P_{\text{HIP}}$ , to the interparticle contact stress  $\sigma_{ij}^*$ , the relationship for the single size case was modified for the bimodal case to give

$$\sigma_{ij}^* = (1/a_{ij}) (\pi P_{\text{HIP}}) / [ (f_1 G_{12}/r_1^2) + (f_2 G_{12}/r_2^2) + (f_1 G_{11}/r_1^2) + (f_2 G_{22}/r_2^2) ] \quad (3)$$

where  $f_1$  and  $f_2$  are the volume fractions of the two different sized particles with respective radii  $r_1$  and  $r_2$ ,  $G_{11}$ ,  $G_{12}$ , and  $G_{22}$  are the coordination numbers 11, 12, and 22, respectively.

Given the above new formulations described by Eqs. (1), (2), and (3), the new model then proceeds to derive for the bimodal case the density as a function of time using the premise that the densification can be modeled by a fictitious growth of the particles around their centers, to a new radius  $r'$

$$D/D_0 = f_1 (r_1'/r_1)^3 + f_2 (r_2'/r_2)^3 \quad (4)$$

The contact stress is used as input for constitutive equations for each mechanism under consideration and used to calculate a densification rate ( $D$ ) for each mechanism. The rates are summed for all mechanisms ( $m$ ) for each particle

size (i), then weighted by number fraction of each particle for a total densification rate:

$$D = \sum_i n_i \sum_n D_{im}. \quad (5)$$

The deformation mechanisms considered are yielding, power law creep, superplasticity, diffusional creep and diffusion. The densification rate equations (shown in Table X) are evaluated for each increment of density at a constant HIP temperature for a range of HIP pressures. The mechanism with the greatest densification rate is considered to be dominant at that HIP pressure and density. The densification rates are summed up and integrated to predict densification kinetics. A flow chart of the model is shown in Figure 16. The data is presented on a HIP map or diagram that shows fields of dominance for each mechanism in HIP pressure and density. The maps can also be created for a constant HIP pressure with a range of HIP temperatures.

The final results of the theory are shown in Figures 17 - 29. It is interesting (see Figure 17) that the interparticle deviatoric stress causing particle deformation is of the order of 0.1 to as high as 100 times the HIP pressure depending on the particle size and the instantaneous density. Further, this deviatoric stress on the smaller particle can be of the order of 1.5 times that on the larger particle. In addition, Figure 18 indicates that the smaller particles undergo the greater degree of plastic deformation relative to their larger counterparts. These results are in contrast to the Arzt et al. model wherein all particles experience the same levels of stress and strain.

As mentioned, the smaller particles in a distribution of particles undergo the greater degree of plastic deformation. The theoretical result is even consistent with the experimental finding. Figure 19 shows a bimodal HIP map for the yield(athermal plastic flow)/power law creep regimes. The small particles

continue to yield longer (to a higher density) than the large particles.

Figures 20 through 26 show modeling of the Year One HIP and CAP runs. For simplicity, the powder was assumed to be of a single average size. Figure 20 shows the experimental kinetic data. Figures 21 and 22 show good agreement between predicted and experimental kinetics for the two HIP conditions (1121°C, 100 MPa and 1121°C, 10 Mpa). Densification which occurs during the heatup/pressurize and cooldown/depressurize was included in the modeling.

Figures 23 and 24 show HIP maps at 1121°C with regimes of yield (APF), power law creep (DC), superplasticity (SP), Nabarro-Herring/Coble (diffusional) creep (NHC) and boundary diffusion (BD). As the average particle size is increased from 9.75  $\mu\text{m}$  for the full size powder distribution to 41.25  $\mu\text{m}$  for monosized powder, densification by diffusion is reduced in favor of Nabarro-Herring/Coble creep.

The experimental CAP data is compared to the HIP model in Figures 25 and 26, with good agreement. Again the heatup and cooldown times were modeled. For the higher temperature CAP run, grain growth and increased boundary thickness caused by the higher temperature and the sintering aid used in CAP were included in the model.

The second year HIP experiments are compared to the bimodal HIP model in Figures 27 and 28. The particle size ratio was taken as 2.3. Figure 29 shows a bimodal HIP map at 1000°C. Each of the regime boundaries have split for the large and small particles, as was shown in Figure 19 for yield/power law creep.

**Table X. Densification Rates for each Mechanism.**

<u>Deformation Mechanism</u>	<u><math>D_0 \leq D \leq 0.9</math></u>	<u><math>0.9 &lt; D \leq 1.0</math></u>
Athermal Plastic Flow (APF)	<p>If <math>P_{eff} \geq 3 \sigma_y</math> then <math>\dot{D} = 1.0 \text{ sec}^{-1}</math></p> <p>If <math>P_{eff} &lt; 3 \sigma_y</math> then <math>\dot{D} = 0</math></p>	<p>If <math>P_{HIP} \geq \frac{2 \sigma_y}{3} \ln \left( \frac{1}{1-D} \right)</math> then <math>\dot{D} = 1.0 \text{ sec}^{-1}</math></p> <p>If <math>P_{HIP} &lt; \frac{2 \sigma_y}{3} \ln \left( \frac{1}{1-D} \right)</math> then <math>\dot{D} = 0</math></p>
Power Law Creep (PLC)	$\dot{D} = \frac{27 \pi (D^2 D_0)^{1/3}}{16 R_0} A \left( \frac{P_{eff}}{3} \right)^n$	$\dot{D} = \frac{3D(1-D)}{2[1-(1-D)^m]^n} A \left( \frac{3P_{HIP}}{2n} \right)^n$
Interparticle Boundary Diffusion (BD)	$\dot{D} = \frac{43(1-D_0)^2 (\delta D_b + \rho D_v)}{(D-D_0)^2 kTR_0^3} \Omega P_{eff}$	$\dot{D} = \frac{270 \sqrt{(1-D)} (\delta D_b + r D_v)}{kTR_0^3} \Omega P_{HIP}$
Nabarro-Herring and Coble Creep (NHC)	$\dot{D} = \frac{24.9 \Omega (D^2 D_0)^{1/3}}{kTG^2 R_0} \left[ D_v + \frac{\pi \delta D_b}{G} \right] P_{eff}$	$\dot{D} = \frac{31.5 \Omega (1-D)}{kTG^2} \left[ D_v + \frac{\pi \delta D_b}{G} \right] P_{HIP}$

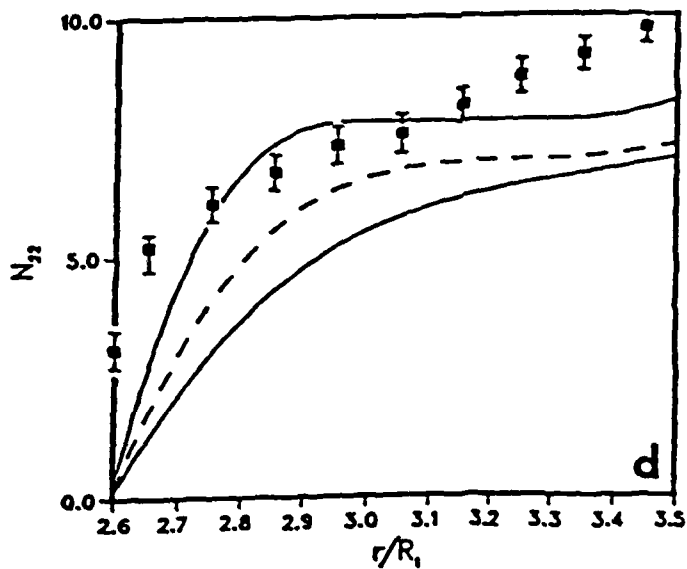
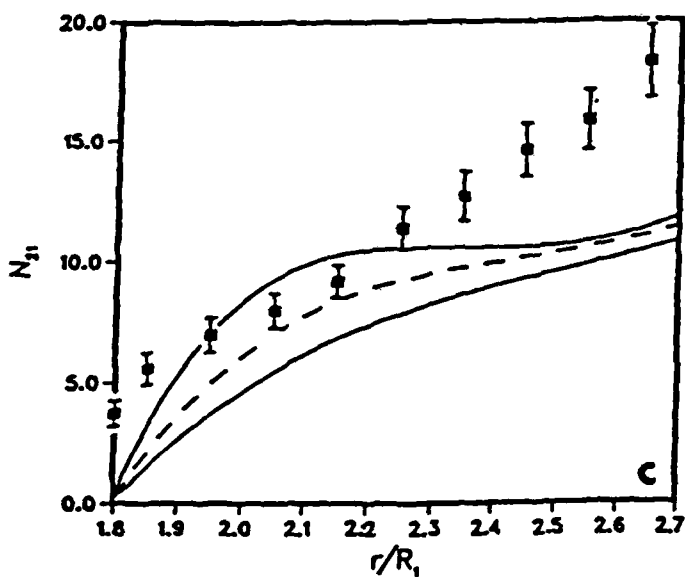
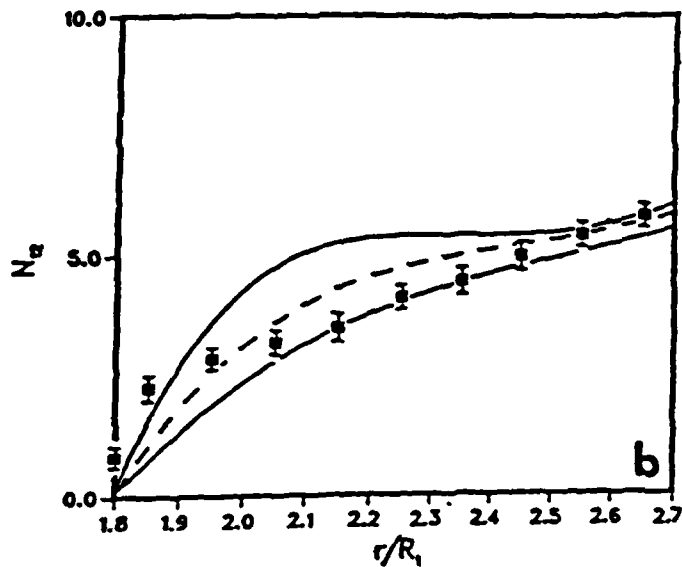
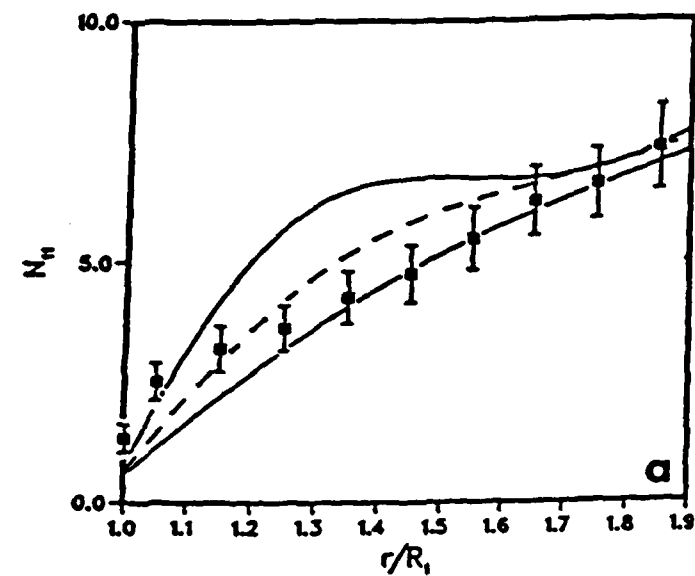


**Figure 15.** Results of the distribution  $N_{ij}$  for the bimodal case with 10% small particles. The solid points are the experimental data points. The lower solid theoretical curve in a) through d) is for  $D_0 = 0.557$  and the upper solid theoretical curve is for  $D_0 = 0.671$ , the measured lower and upper bounds for  $D_0$  (the initial powder density). The dashed curve is the analytical result for the average density value of 0.61. All radial distances are normalized to the small particle diameter  $R_1$ .

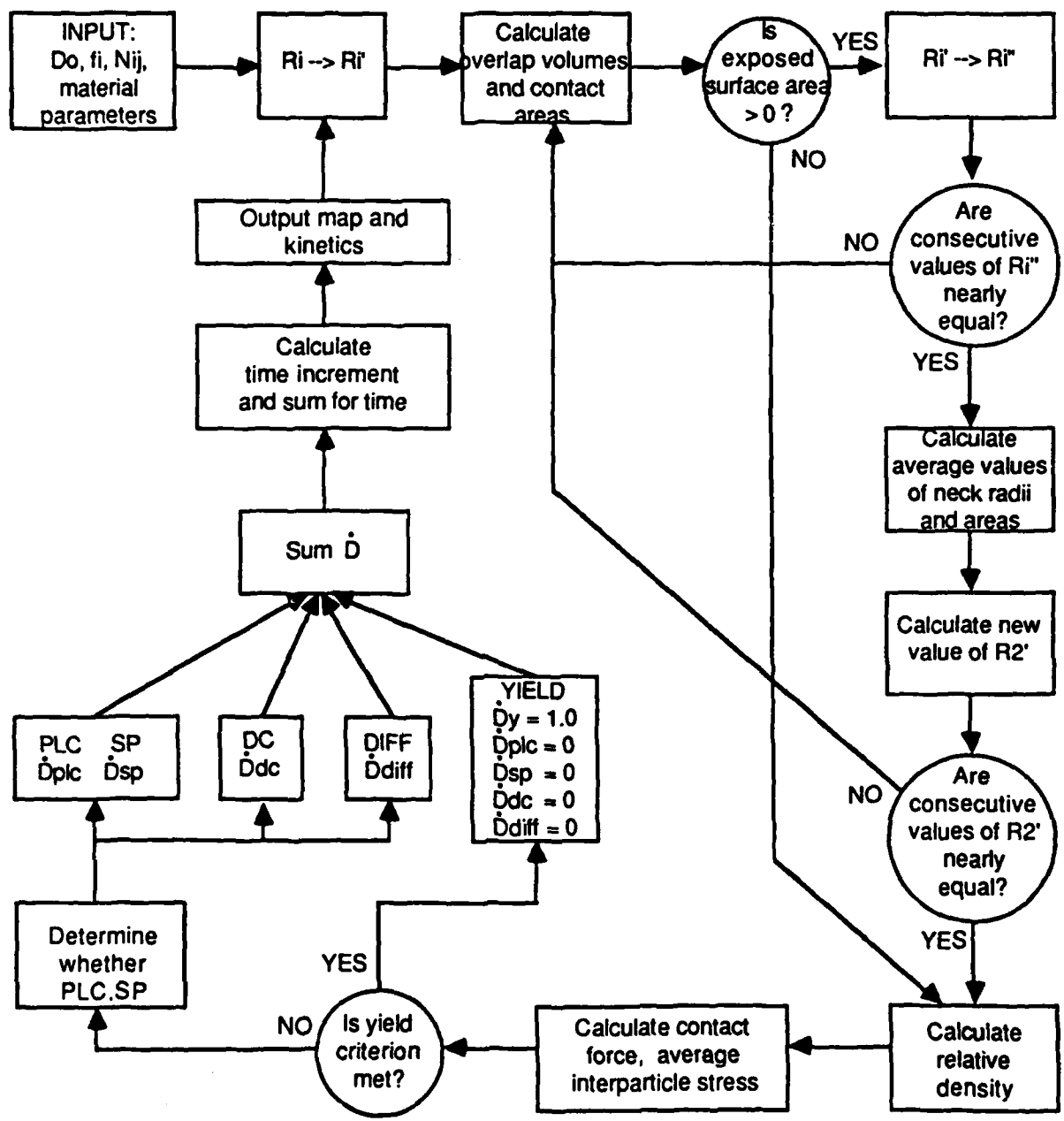
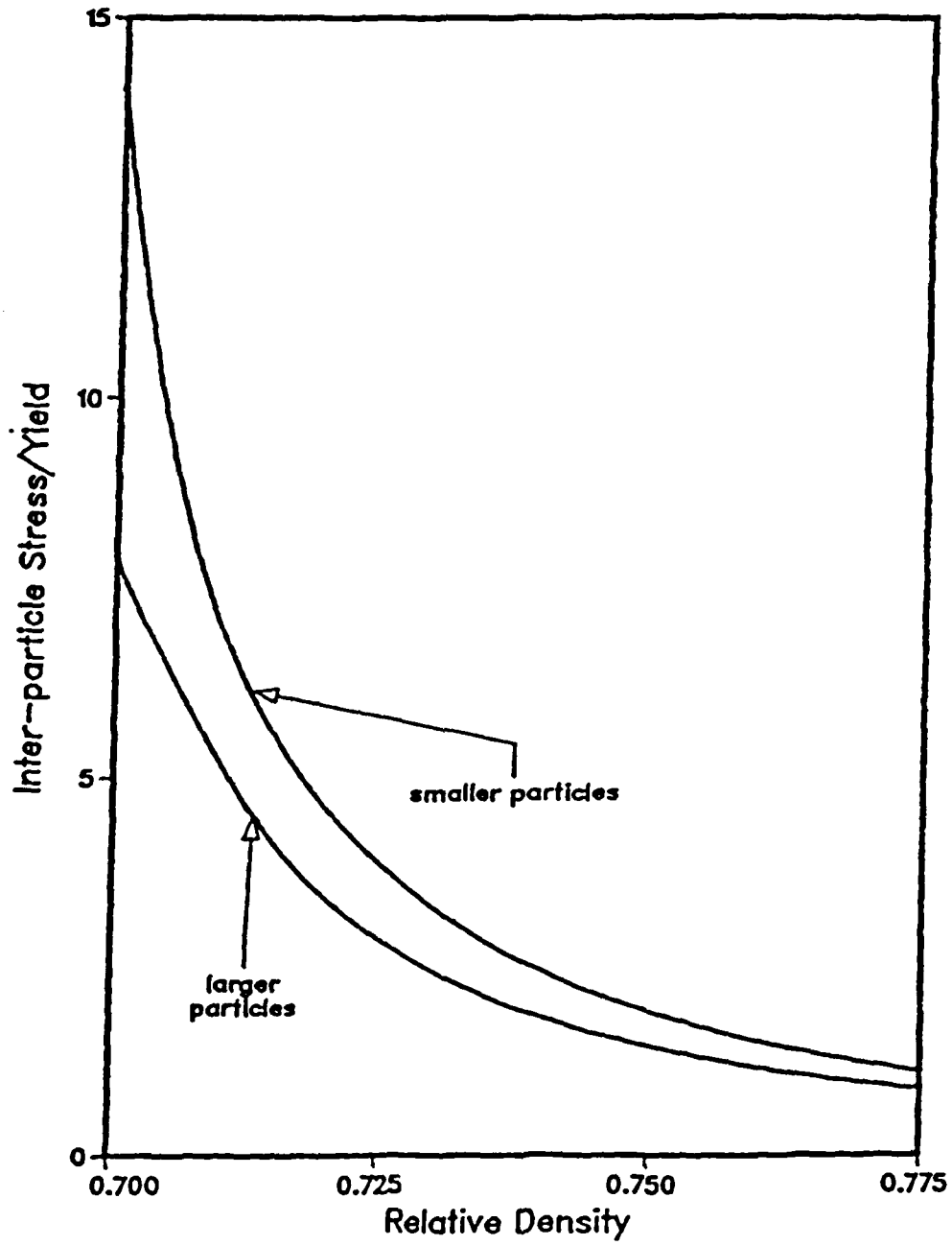
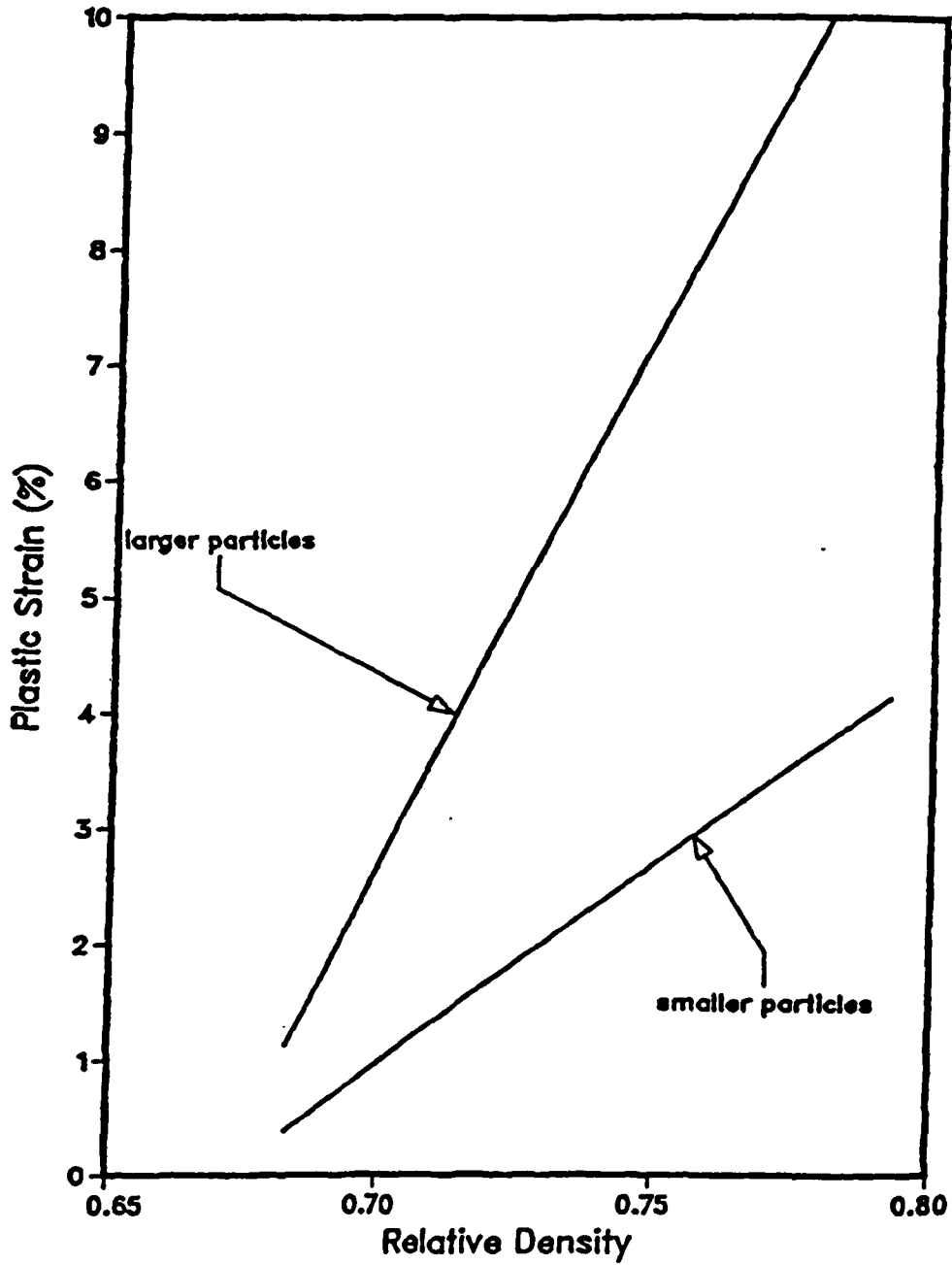


Figure 16. Flow chart of bimodal HIP model.



**Figure 17.** Interparticle contact stresses experienced by smaller and larger particles during HIP of a bimodal size distribution of powders [ $\log(P/Y) = -1.0$ ,  $T = 1121^\circ\text{C}$ ].



**Figure 18.** Plastic strain suffered by smaller and larger particles during HIP of a bimodal particle size distribution of powders [ $\log(P/Y) = -1.0$ ,  $T = 1121^\circ\text{C}$ ].

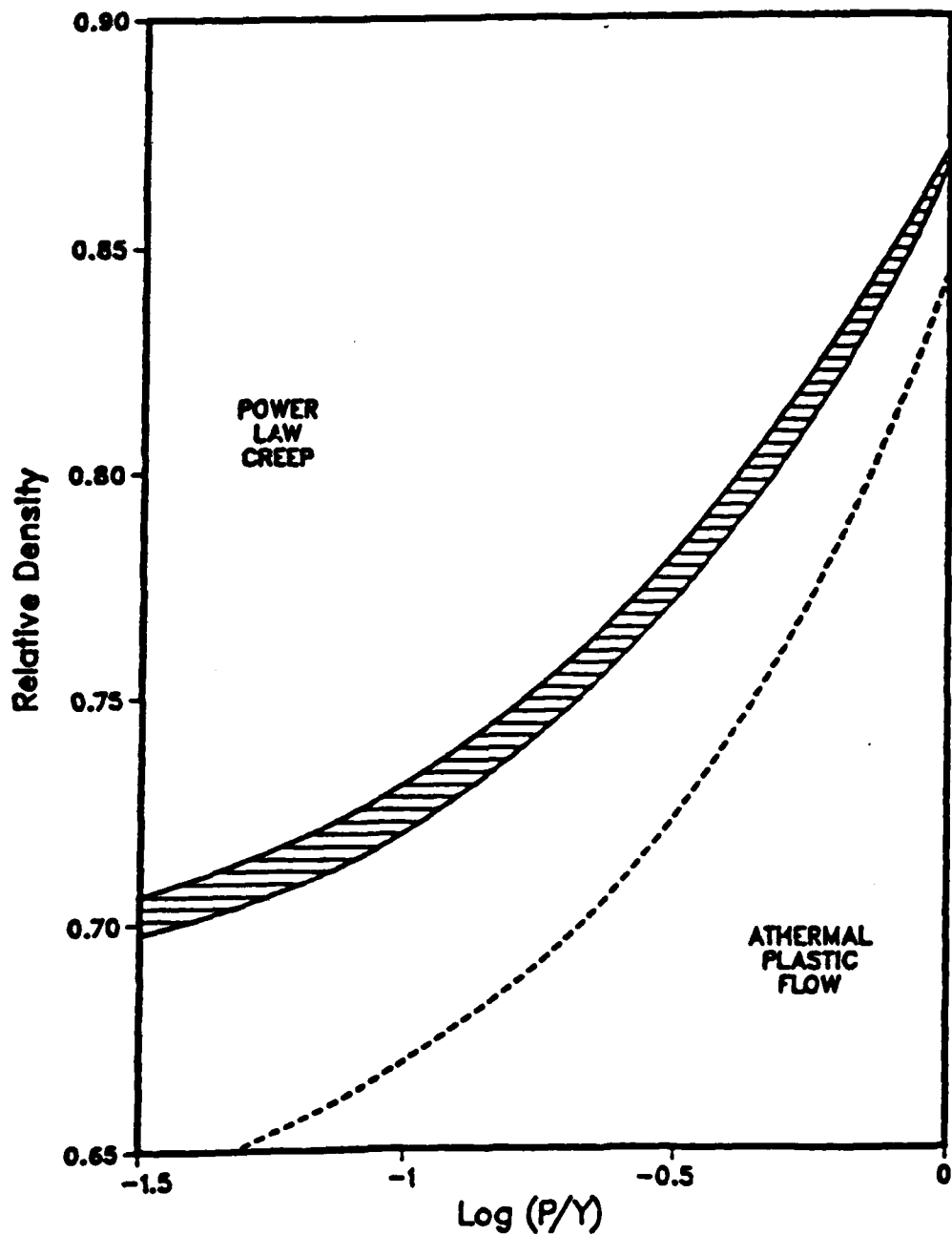


**Figure 19.** Boundary between the power-law creep and athermal plastic flow regions in a HIP densification map. The dashed line is as calculated by Arzt et al. for deformation of single sized particles. The upper solid line is for the smaller particles and the lower solid line is for the larger particles [ $T = 1121^{\circ}\text{C}$ , particle size ratio = 2.3, and weight percent of smaller particles = 20%].

P/M RENE'95  
EXPERIMENTAL DENSIFICATION DATA

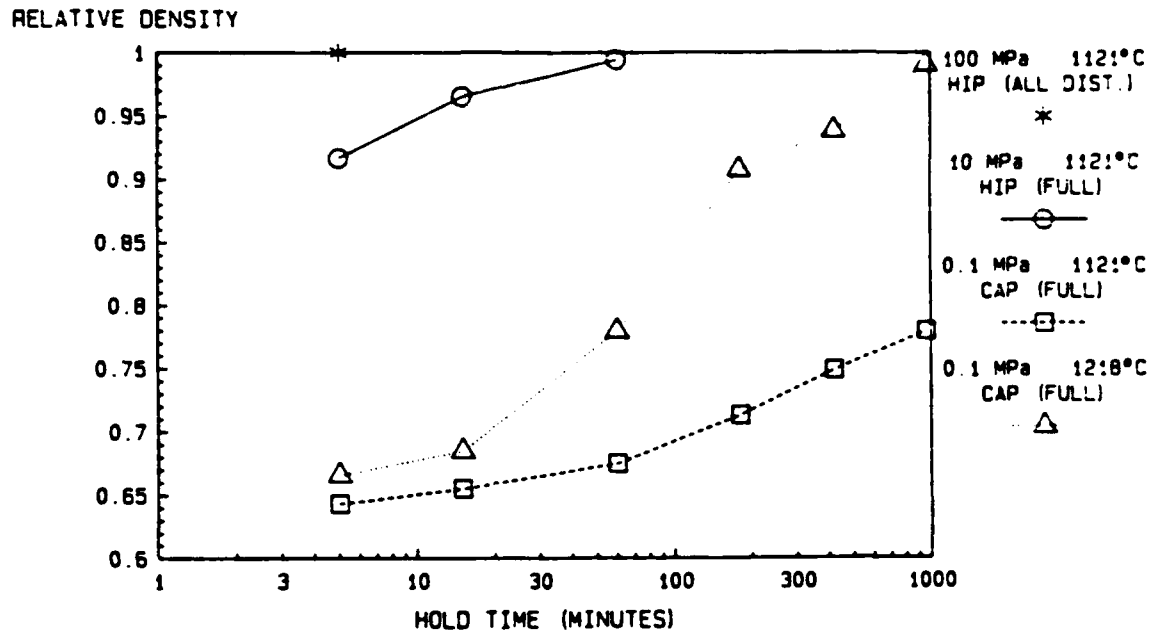


Figure 20. Experimental HIP densification data.

RENE '95 HIP DENSIFICATION  
100 MPa 1121°C

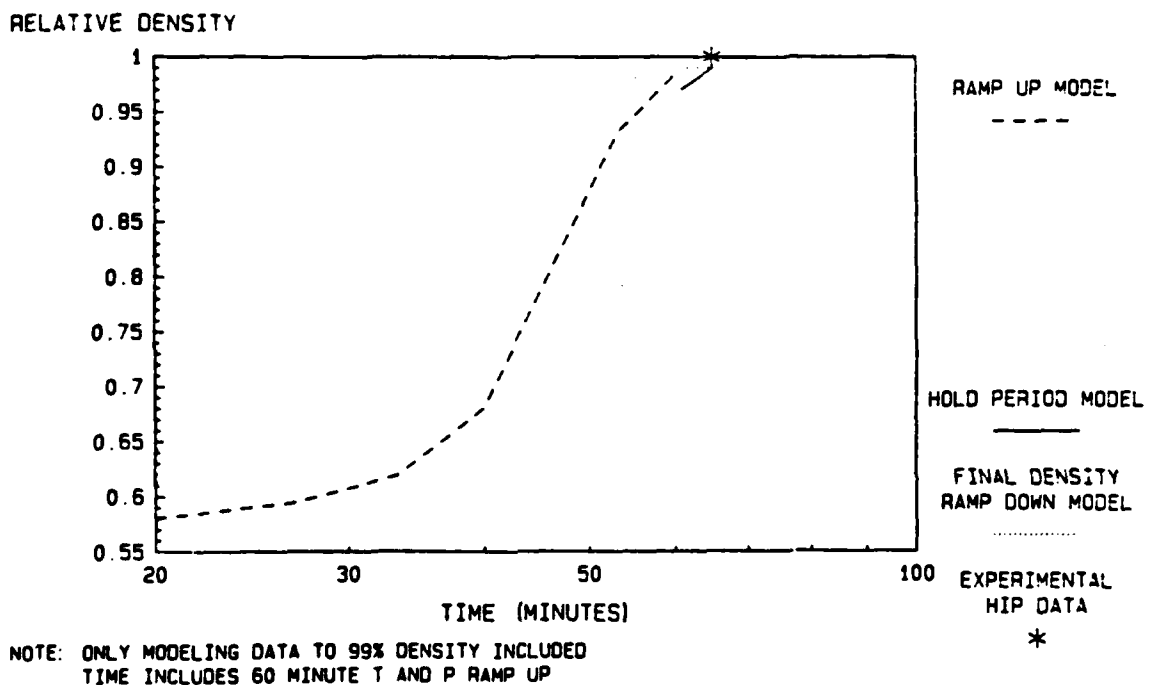
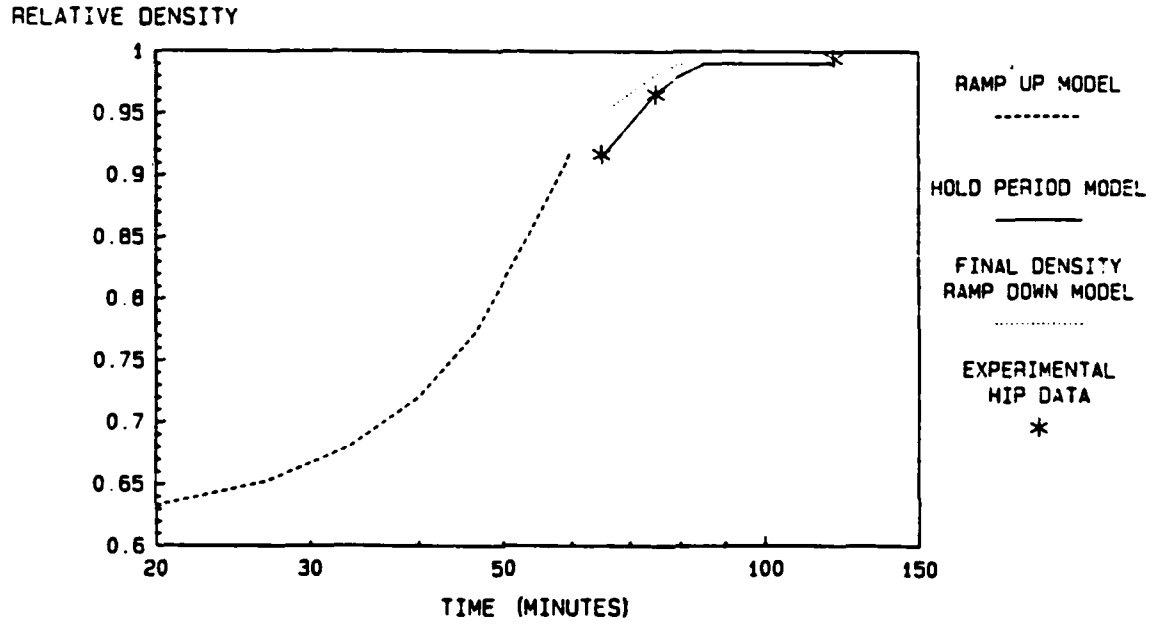


Figure 21. Modeling of Rene 95 HIP densification at 100 MPa and 1121°C.

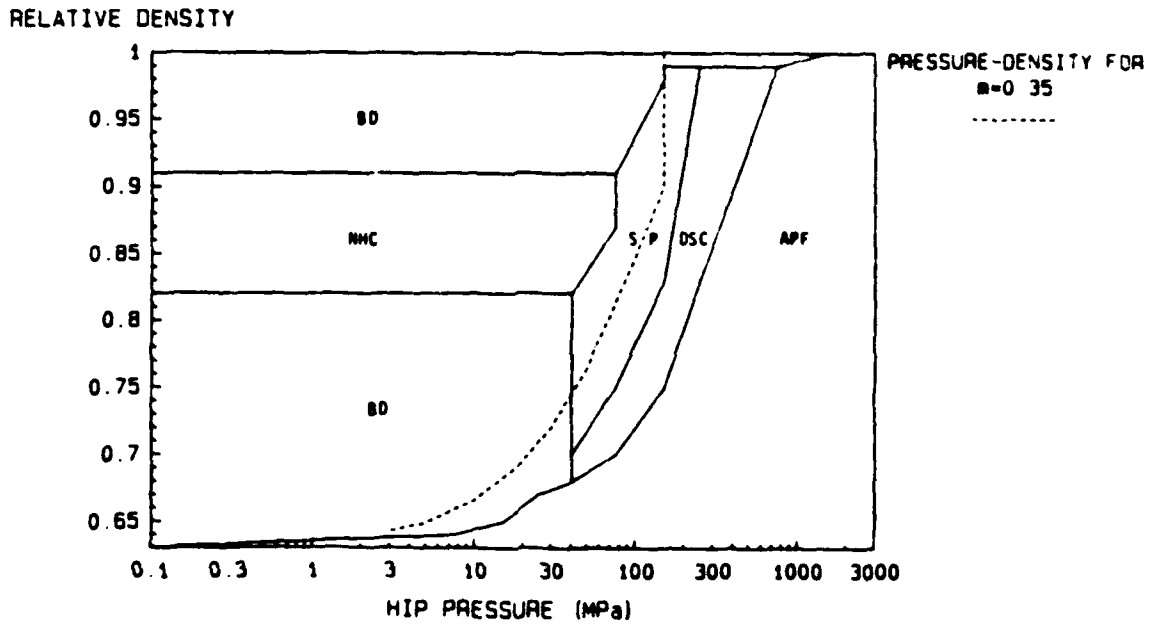
RENE '95 HIP DENSIFICATION  
10 MPa 1121°C



NOTE: ONLY MODELING DATA TO 99% DENSITY INCLUDED  
TIME INCLUDES 60 MINUTE T AND P RAMP UP

Figure 22. Modeling of Rene 95 HIP densification at 10 MPa and 1121°C.

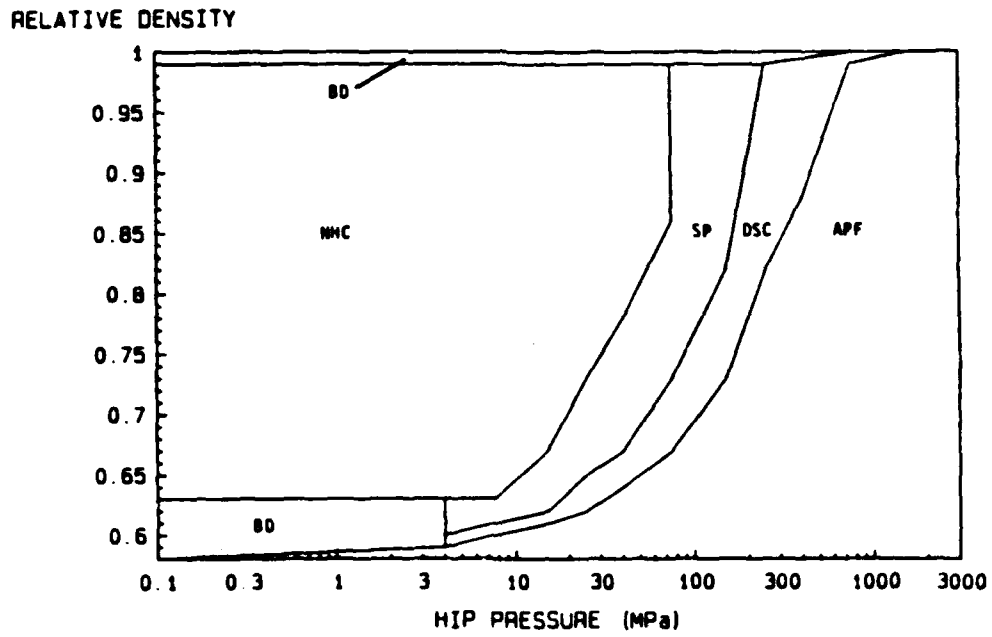
RENE'95 DENSIFICATION MECHANISM MAP  
 FULL PARTICLE DISTRIBUTION  
 1121°C



NOTE: 9.75  $\mu\text{m}$  AVERAGE PARTICLE DIAMETER  
 5  $\mu\text{m}$  GRAIN SIZE

Figure 23. Rene 95 HIP densification mechanism map for a full distribution of powder at 1121°C.

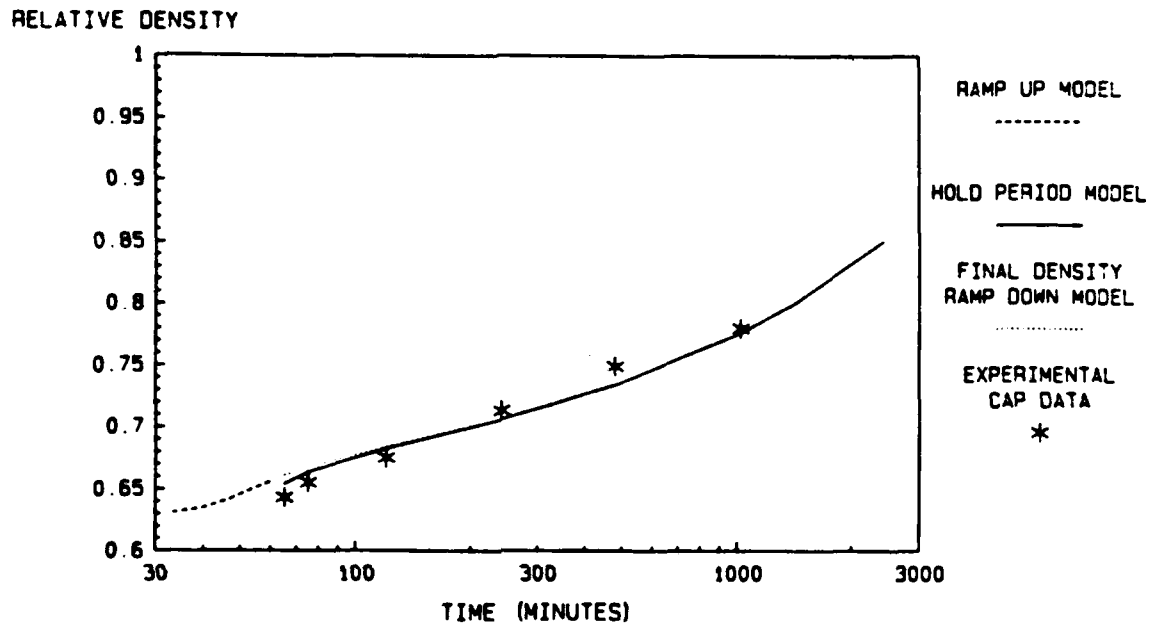
RENE '95 DENSIFICATION MECHANISM MAP  
MONOSIZE PARTICLE DISTRIBUTION  
1121°C



NOTE: 41.25  $\mu\text{m}$  PARTICLE DIAMETER  
5  $\mu\text{m}$  GRAIN SIZE

Figure 24. Rene 95 HIP densification mechanism map for a monosized distribution of powder at 1121°C.

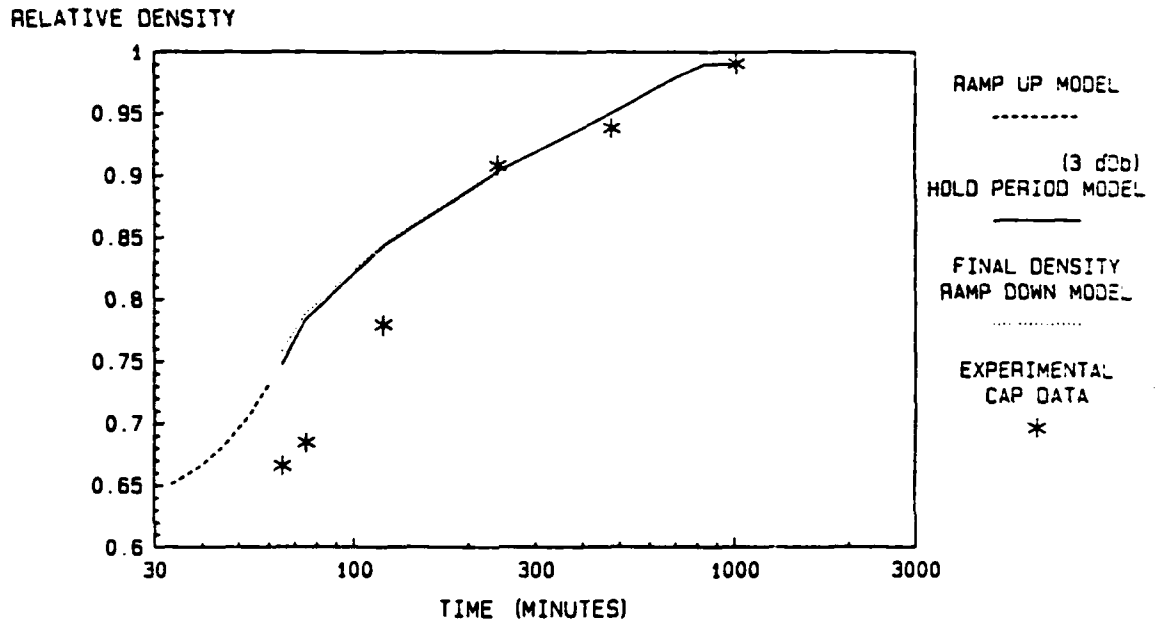
RENE'95 HIP DENSIFICATION  
0.1 MPa 1121°C  
(R=41.25µm G=9µm)



NOTE: ONLY MODELING DATA TO 99% DENSITY INCLUDED  
TIME INCLUDES 60 MINUTE T AND P RAMP UP

Figure 25. Modeling of Rene 95 CAP densification at 0.1 MPa and 1121°C.

RENE '95 HIP DENSIFICATION  
 0.1 MPa 1218°C  
 (3 dDb)



NOTE: ONLY MODELING DATA TO 99% DENSITY INCLUDED  
 TIME INCLUDES 60 MINUTES T AND P RAMP UP

Figure 26. Modeling of Rene 95 CAP densification at 0.1 MPa and 1218°C.

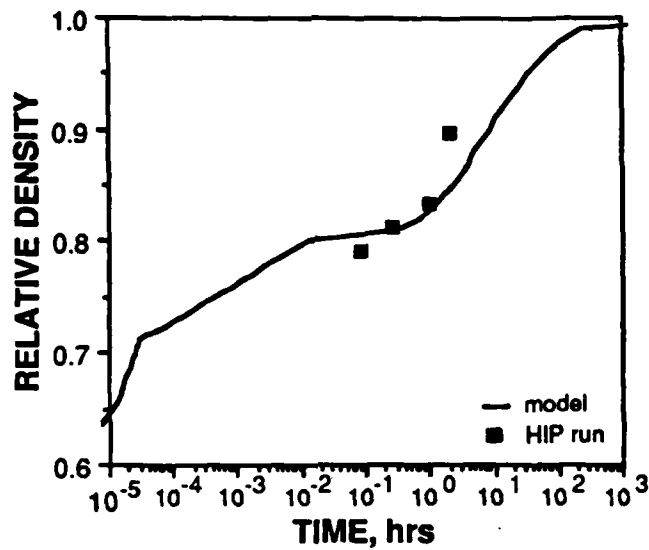


**Figure 27.** Bimodal modeling of Rene 95 HIP densification at 100 MPa and 900°C.

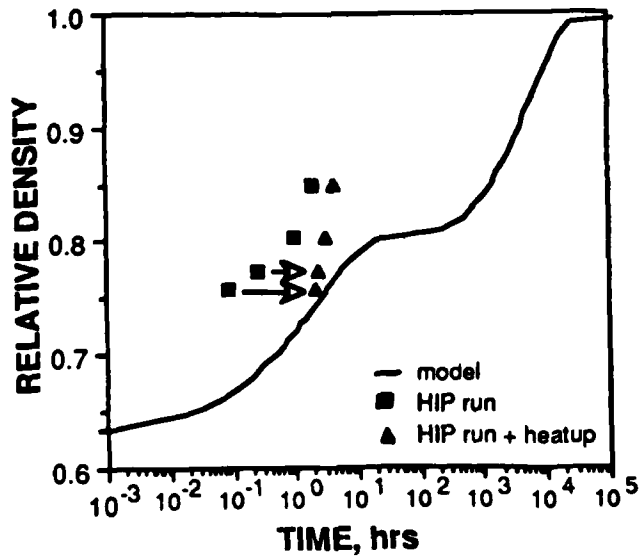


**Figure 28.** Bimodal modeling of Rene 95 HIP densification at 10 MPa and 1000°C. When the heatup time is taken into consideration, the predicted kinetics are closer to the experimental data.

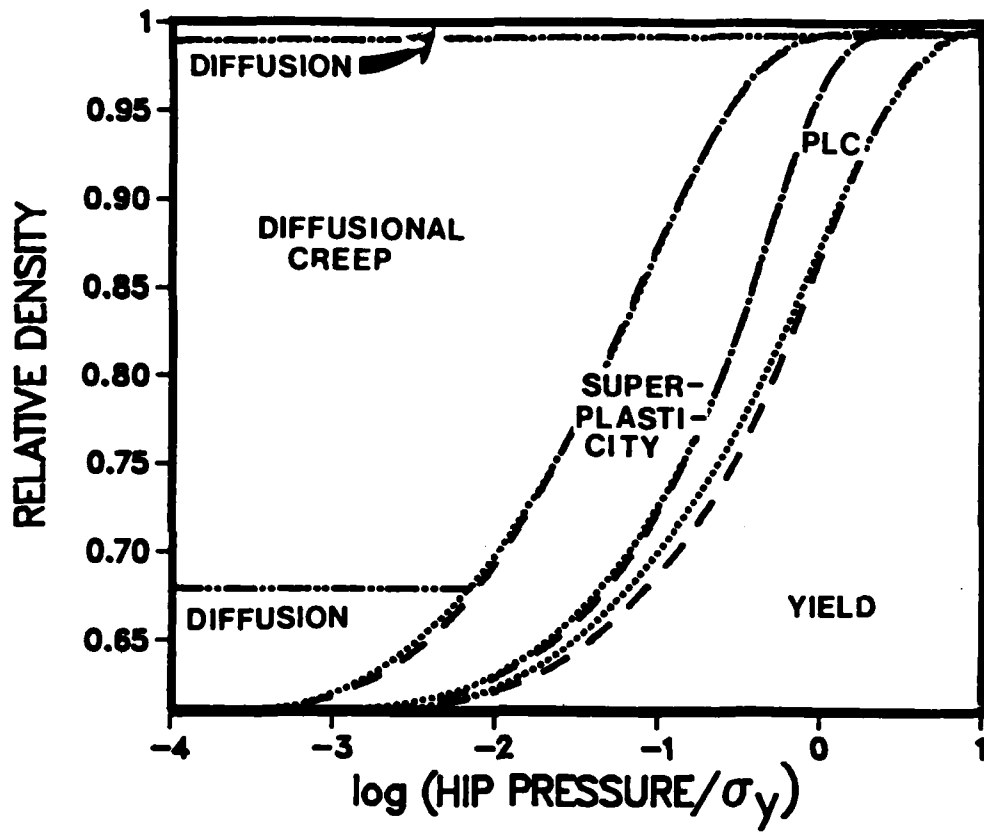


Figure 29. Bimodal HIP map for Rene 95 (weight fraction of small particles = 10%, particles size ratio = 2.3 and HIP temperature = 1000°C).

#### F. Variable Pressure HIP Runs

In an effort to maximize and equalize deformation by all particles, variable HIP pressure runs were done. This is done to maintain HIP densification by a single dominating mechanism, especially by a mechanism such as superplasticity which is well-characterized in its uniformity of deformation over varying areas or gauge lengths. If the HIP pressure is varied during the HIP run, a particular mechanism can be allowed to dominate for the entire duration of the run, as shown in Figure 30. If HIP pressure is held constant during a HIP run, several mechanisms operate, each for a small range of the densification process. The variable pressure HIP runs were done with full size and monosize powder. All HIP runs resulted in fully dense material. Table XI shows the HIP conditions used. Figure 31 shows the microstructure of the material HIPed at 1000°C, from 21 MPa to 48 MPa in 8 hours. The deformation of all particles appears to be more uniform.

**Table XI. Variable Pressure HIP Runs**

HIP T, °C	Starting HIP P, MPa	Ending HIP P, MPa	Ramping Rate, MPa/min	Duration of Ramp, min
1000	21	48	1.7/60	240
1000	21	48	1.7/30	480
1050	21	34	1.6/60	240
1050	21	34	1.6/30	480

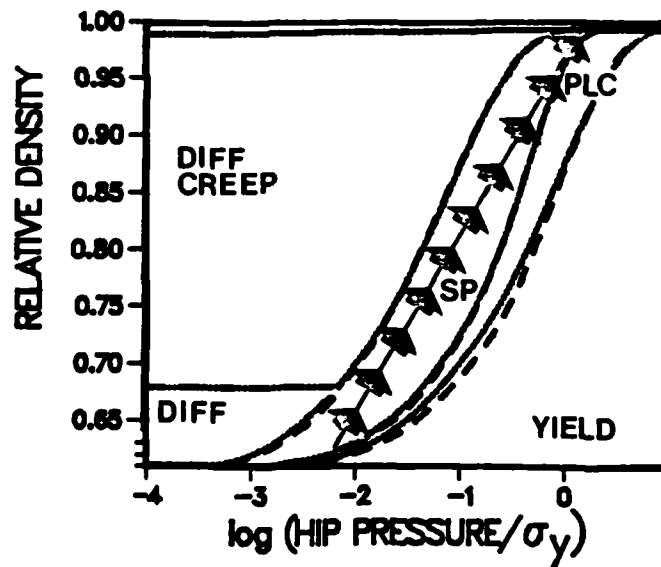


**Figure 30. Schematic of ramped HIP pressure run.**

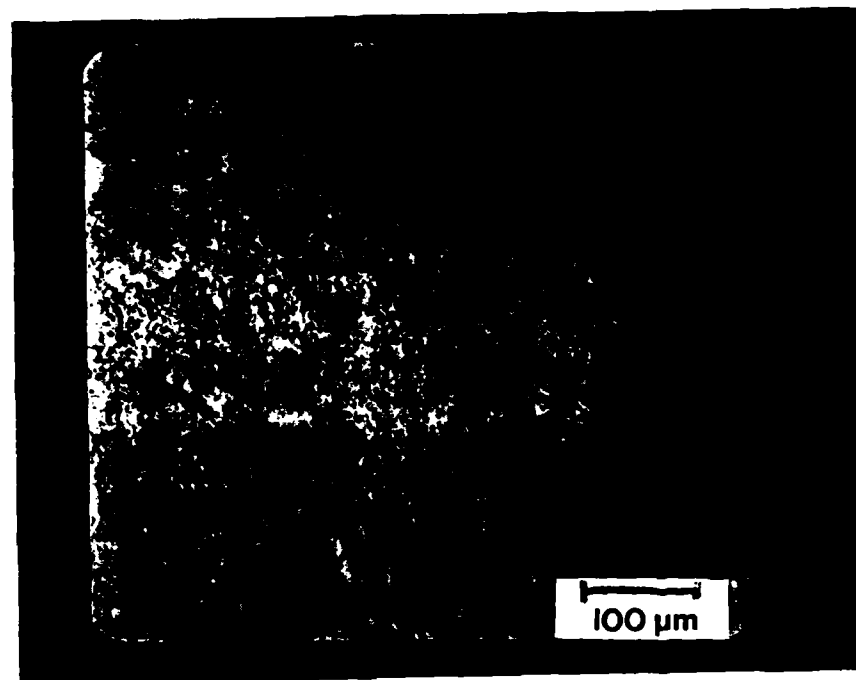


**Figure 31.** Microstructure of material consolidated by ramped HIP pressure run.

## G. Modeling of HIP of Oxide Superconductors

The effects of material and powder input parameters on HIP modeling were investigated using the new material system of oxide superconductors.

Bulk shapes of the high  $T_c$  oxide superconductors ( $YBa_2Cu_3O_{7-x}$  (F)) are commonly produced by the sintering of the precursor powders. The sintered material, even when processed at the highest appropriate temperature for a day or more, is only 80-90% dense. Reliable applications of brittle materials require fully dense material. This would be the case either for preforms for subsequent extrusions into cables or wires, or for such applications of shaped superconductors as magnets, rails, bearing races, and storage rings. Hot Isostatic Pressing (HIP) of these high  $T_c$  oxides will allow the fabrication of fully dense bulk shapes. As will be discussed later, aside from solving the consolidation problem, HIP processing may yield other dividends with respect to accelerating the commercialization of superconductor shapes.

Effect of Temperature and Pressure: Figure 32 shows a HIP densification map for monosized 50  $\mu$ m diameter powder at 900°C. The map shows the effect of HIP pressure and the relative contribution of each of the hot deformation and diffusion mechanisms. As would be expected, as the HIP pressure is increased, higher density is reached by rapid hot yielding and the time to reach a particular density is consequently shorter. In Figure 32a, at 1000 MPa, it is seen that full densification is predicted to occur in less than 15 minutes. At that pressure, about 90% density is reached by hot yielding which is nearly instantaneous. The rest of the densification is expected to occur by creep deformation. This rapid densification is in contrast to current sintering consolidation where no pressure is applied. As mentioned, sintering does not

result in full densification even after 24 hours at 900°C. Likewise, if a very low HIP pressure is used, for example 0.1 MPa in Figure 32a, full densification is not expected even after very long times. Densification at these low pressures occurs mainly by Nabarro-Herring/Coble (diffusional) creep, which is much slower than the hot yielding mode. At an intermediate HIP pressure, such as 1.0 MPa, in Figure 3a, densification occurs by a combination of power law and diffusional creep, and full densification can be reached in reasonable time (about 16 hours).

The sensitive effect of HIP temperature is seen by a comparison of Figures 32a and 32b, which are HIP maps at 900°C and 750°C, respectively. A HIP pressure of 100 MPa at 900°C results in full density in less than 15 minutes. At 750°C, full densification takes about 4 hours. The hot yield regime boundary does not move in this series of maps since, as discussed, the yield strength has been assumed to be constant with temperature.

Effect of Powder Particle Size: In sintering, reducing the powder particle size can somewhat increase the densification rate. This is confirmed by comparing the low pressure regions of Figures 32a and 33 where bulk diffusion is the controlling densification mechanism. Decreasing the powder particle size from 50  $\mu\text{m}$  (Figure 32a) to 5  $\mu\text{m}$  (Figure 33) increases the density after 4 hours from 87% to 90% at 0.1 MPa. At HIP pressures approaching 10 MPa, where yield and power law creep dominate the densification kinetics, the effect of particle size on densification kinetics reduces to zero.

Effect of Grain Size: The only grain size dependent densification mechanism considered in this work is Nabarro-Herring/Coble (diffusional) creep. Our analysis shows that when the grain size is increased, diffusional creep dominates densification only at low HIP pressures (below 1 MPa). For example,

compare Figures 32a and 34 for 50  $\mu\text{m}$  powder with 0.5  $\mu\text{m}$  and 5  $\mu\text{m}$  grain size respectively. Densification kinetics are affected by the slowed diffusional creep densification. At 1 MPa, 0.5  $\mu\text{m}$  grain size powder reaches full density, but 5  $\mu\text{m}$  grain size powder only reaches about 90% density at 900°C in 16 hours.

Effect of Entrapped Gas: One of the potential advantages of HIP is the incorporation of reactive gases in the densification process. However, there is a deleterious effect of entrapped gas pressure on HIP densification. This is illustrated at 900°C for 50  $\mu\text{m}$  particles by comparing Figure 32a to Figures 35a and 35b. Entrapped gas pressures are labeled by their room temperature values; the actual pressure at HIP temperature is much higher. An entrapped gas pressure of only 0.1 MPa (Figure 35a) prevents densification above 99%, because the gas pressure opposing the HIP pressure results in a decrease of contact stresses. If the entrapped gas pressure is 10 MPa, densification is stalled at much lower densities, Figure 32b. Accordingly, care must be taken to ensure that reactive gases in the HIP container react completely with the powders during the HIP consolidation process.

Preliminary Experimental Verification: Powder of  $\text{YBa}_2\text{Cu}_3\text{O}_7$  was produced by calcining  $\text{Y}_2\text{O}_3$ ,  $\text{BaCO}_3$ , and  $\text{CuO}$ . A compact of this powder, which was initially 64% dense and averaged 50 $\mu\text{m}$  in diameter, was subsequently sintered at 900°C for 16 hours after which it was 65% dense. A second sintered tablet was encased in OFHC copper which acts as a HIP can. The can was not degassed. The tablet was then HIPed at 750°C and 100 MPa for 2 hours and slow cooled after which its density was 96% of full density. Densities were determined by point counting. This provides two data points at which to roughly validate the HIP map input parameters.

Figure 36a is a HIP map used to model the sintering of 50  $\mu\text{m}$  powder at 900°C

with an entrapped gas pressure of 0.1 MPa ( 1 atmosphere ). Only densification by diffusion is considered to operate under sintering conditions. On this map, a HIP pressure of 0.1 MPa is roughly equivalent to sintering. The data point for powder sintering for 16 hours shows good agreement with the predicted density. Figure 36b is a HIP map for 50  $\mu\text{m}$  powder at 750 $^{\circ}\text{C}$ . The data point for powder HIPed at 100 MPa for 2 hours again shows good agreement with the predicted density.

Superconductor  $\text{YBa}_2\text{Cu}_3\text{O}_{7-x}$   
 $T=900^\circ\text{C}$ ,  $R=50\ \mu\text{m}$ ,  $GS=0.5\ \mu\text{m}$

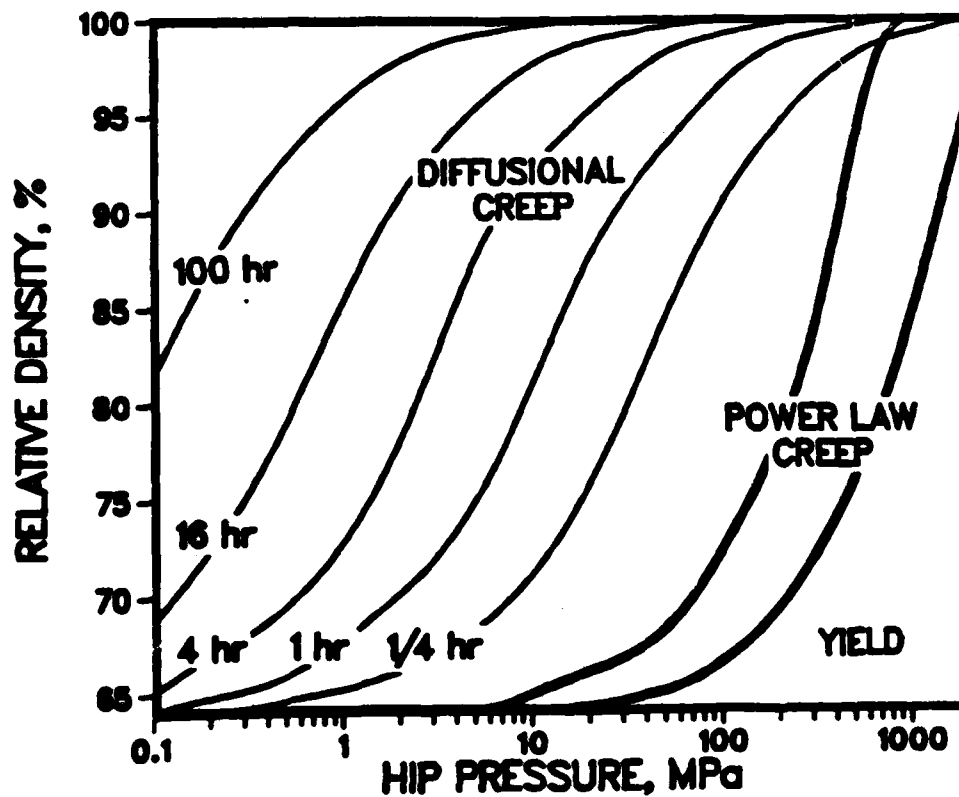
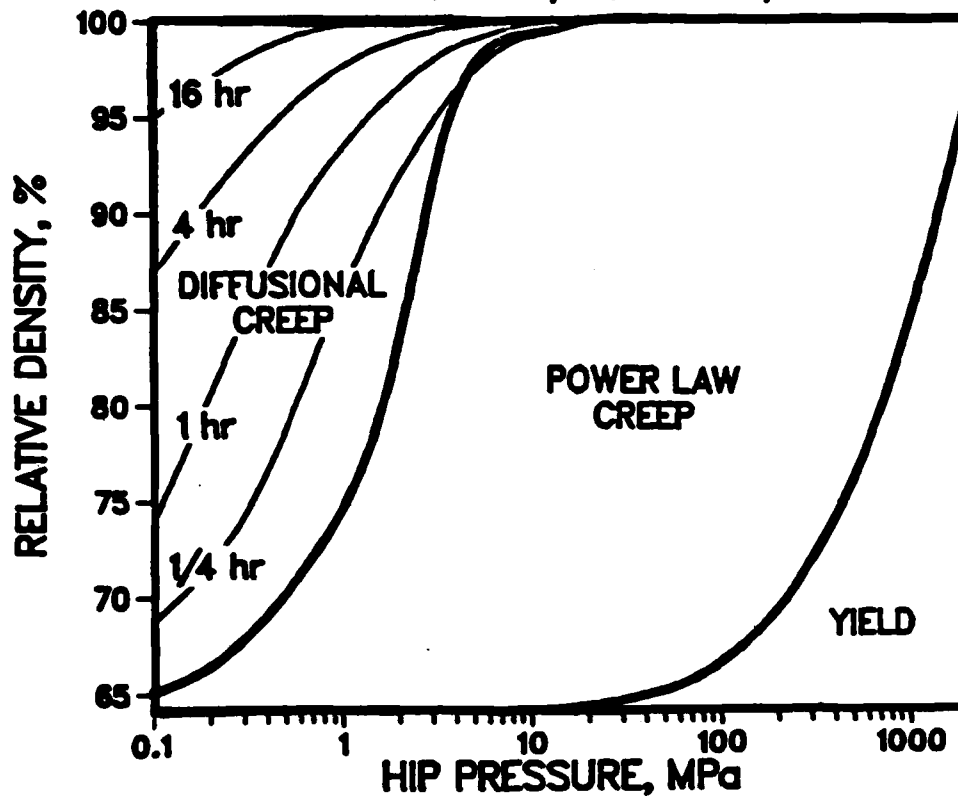
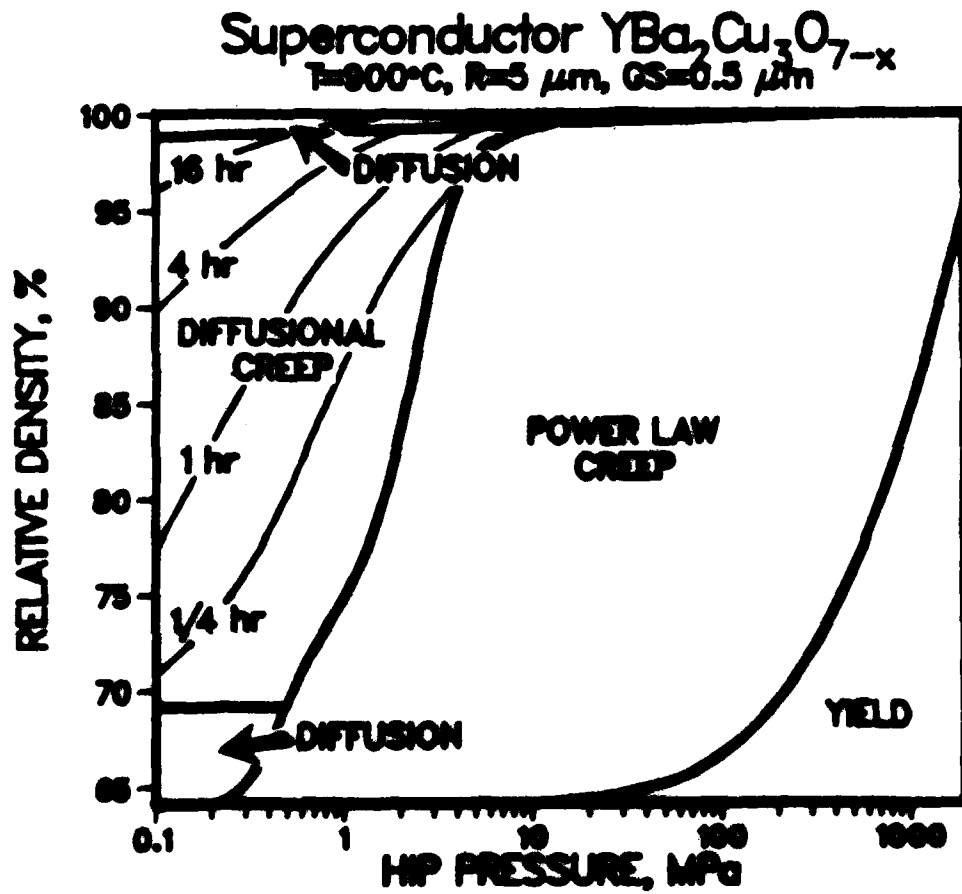


Figure 32. HIP map for monosized  $50\ \mu\text{m}$  powder,  $0.5\ \mu\text{m}$  grain size  $\text{YBa}_2\text{Cu}_3\text{O}_7$  at a)  $900^\circ\text{C}$  and b)  $750^\circ\text{C}$ . The density as a function of pressure is shown for constant time at 15 minutes and 1, 4, 16, 100 hours. The isochronal lines are extrapolated to 100% above 99% density. As temperature decreases, densification is slowed.



**Figure 33.** HIP map for monosized  $5\ \mu\text{m}$  powder,  $0.5\ \mu\text{m}$  grain size  $\text{YBa}_2\text{Cu}_3\text{O}_7$  at  $900^\circ\text{C}$ . The densification by diffusion is enhanced for the small particle size as compared to Figure 32a.

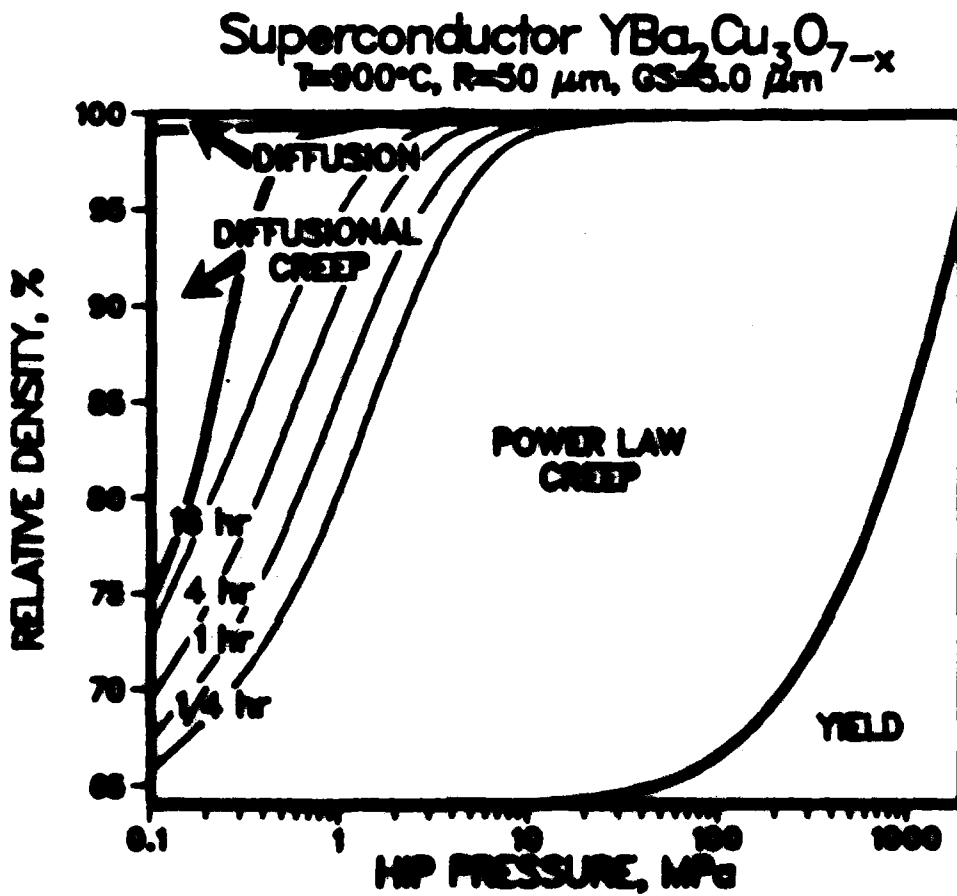


Figure 34. HIP map for monosized  $50\ \mu\text{m}$  powder,  $5.0\ \mu\text{m}$  grain size  $\text{YBa}_2\text{Cu}_3\text{O}_7$  at  $900^\circ\text{C}$ . Diffusional creep dominates only at very low pressures compared to Figure 32a.

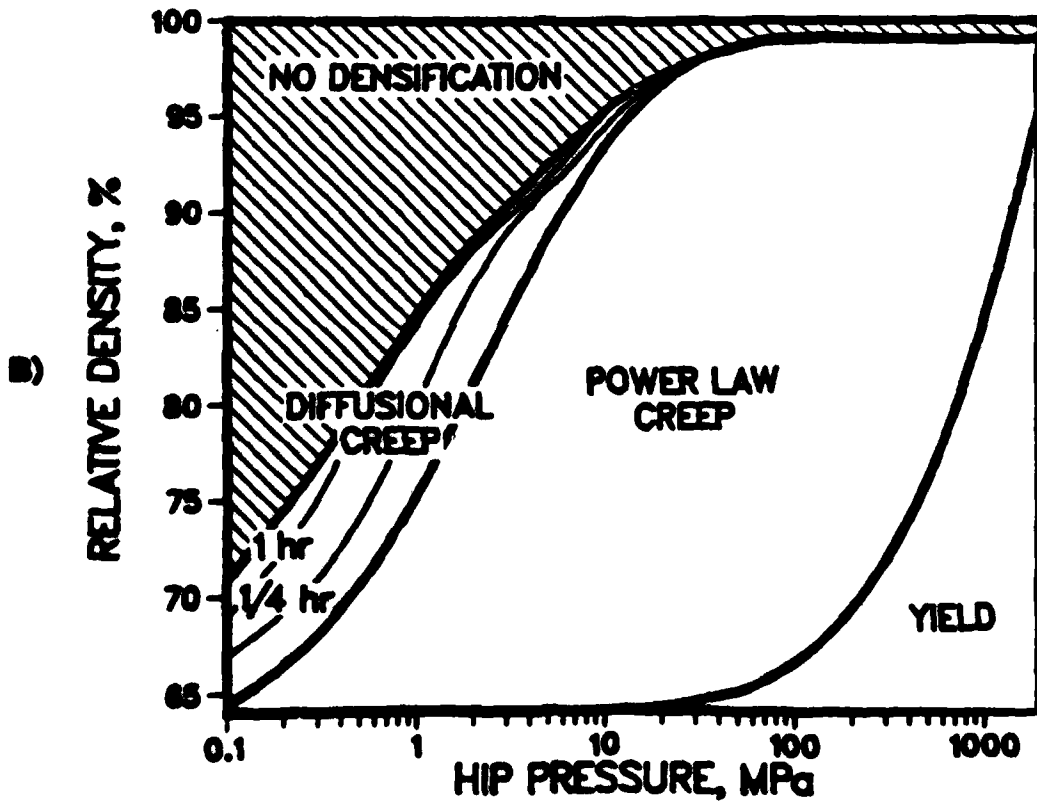
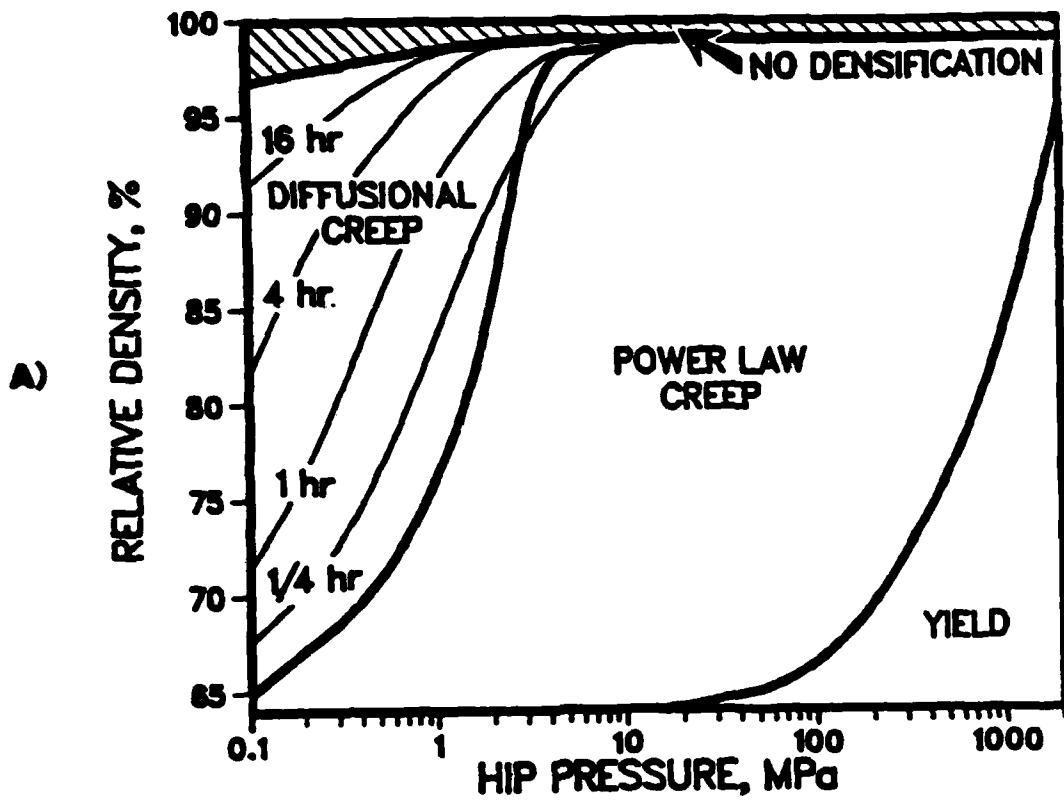
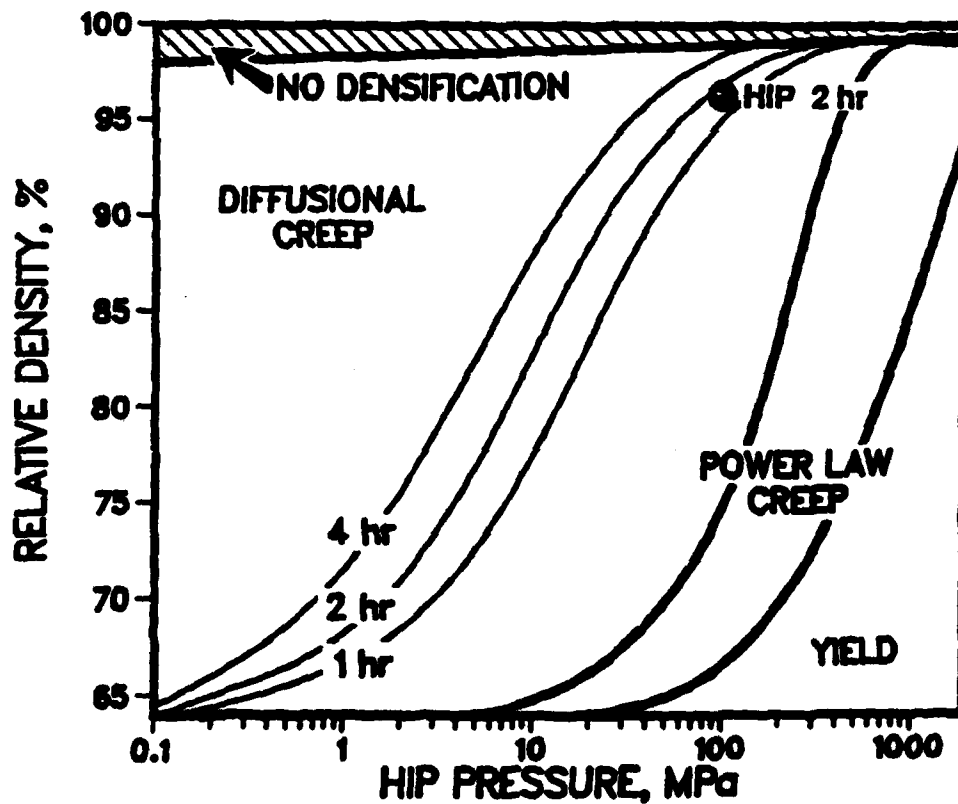
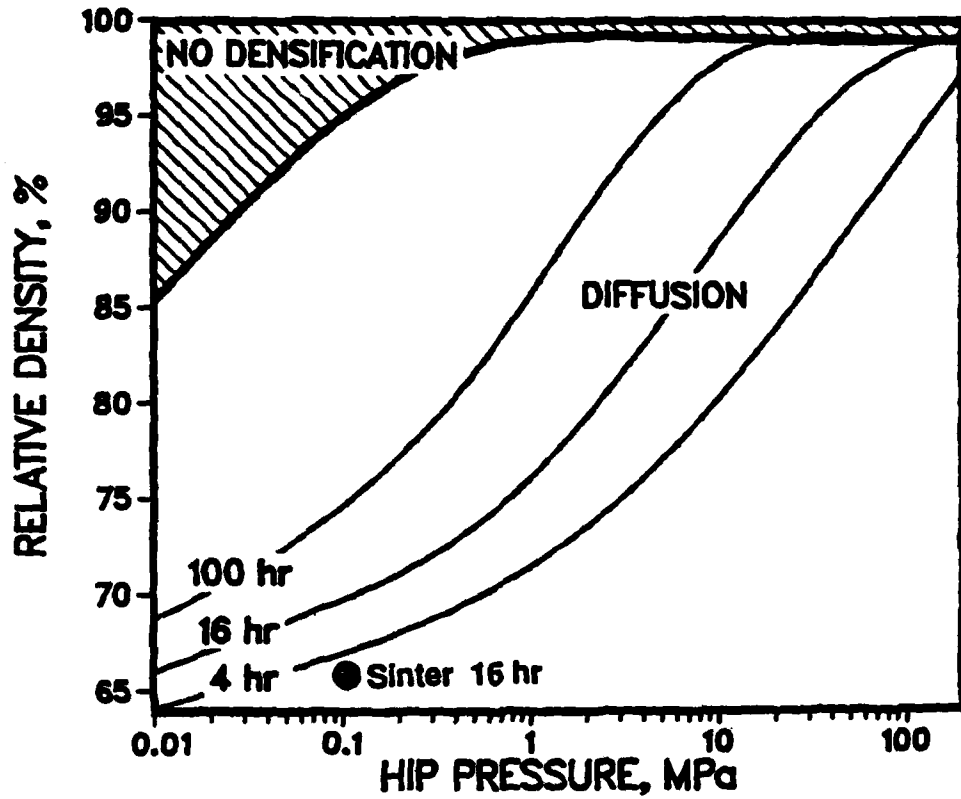


Figure 38. HIP map for monosized 50  $\mu\text{m}$  powder, 0.5  $\mu\text{m}$  grain size  $\text{YBa}_2\text{Cu}_3\text{O}_7$  at 900°C with an entrapped gas pressure of a) 0.1 MPa and b) 10 MPa, which halts densification before 100%.



**Figure 36.** HIP map for monosized 50  $\mu\text{m}$  powder, 0.5  $\mu\text{m}$  grain size  $\text{YBa}_2\text{Cu}_3\text{O}_7$  at experimental conditions: a) sintering at 950°C for 16 hours, 0.1 MPa entrapped gas and b) HIP pressure of 100 MPa at 750°C, 2 hours hold time, 0.1 MPa entrapped gas. Agreement is quite good.

## H. Modeling of HIP of Composites

The bimodal HIP model has been extended to consider densification of particulate composites. The model easily treats HIP of a bimodal mixture of powder materials of equal or different diameters. Each equation is summed for both particles, however for each powder the material parameters are different. The geometry remains the same. For example, for densification by yielding, the densification rate equation becomes:

$$D_{iy} = \begin{cases} 0 & \sigma_{ij}^* < \sigma_{yi} \\ 1 & \sigma_{ij}^* > \sigma_{yi} \end{cases} \quad (6)$$

Figure 32 shows a HIP map for Al-2024/SiC.

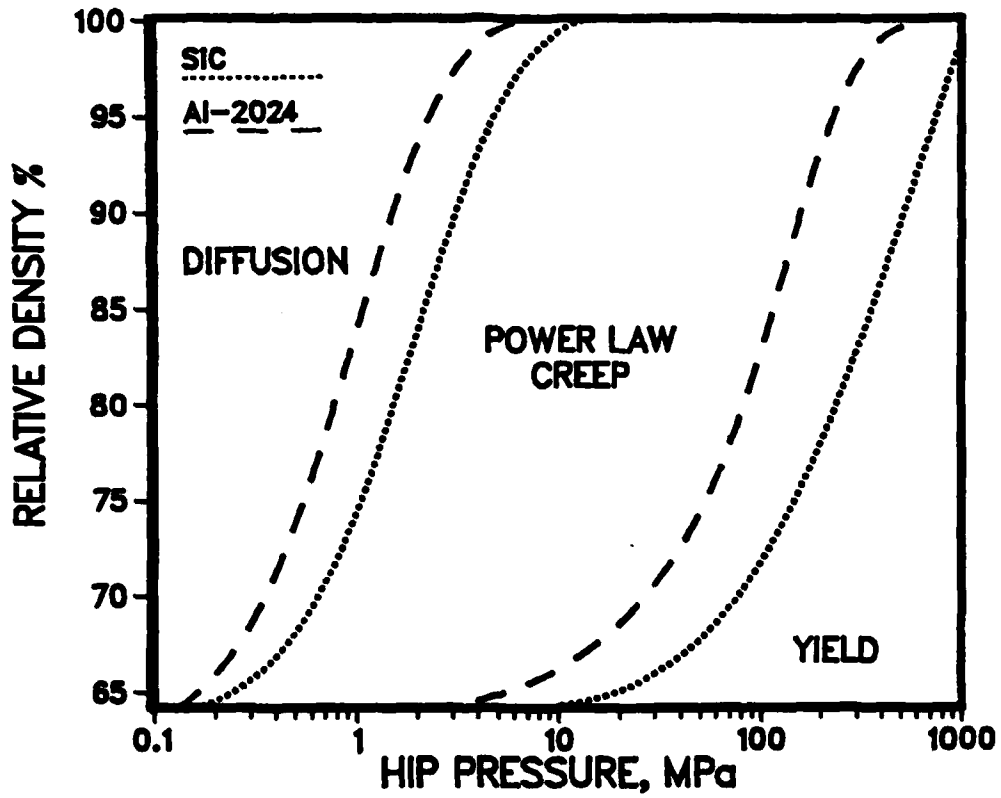


**Figure 37.** HIP map for Al-2024/SiC reinforced composite,  $T=400^{\circ}\text{C}$ , particle size ratio = 5, small (SiC) particle weight percent = 10%.

### III. Theses from This Research

#### Bachelors Degree

Choon Ho Lee	October 1982
Bryan Hendrix	January 1985
Sharon Ventura	May 1986

#### Masters Degree

Barbara Naylor	May 1982
Robert Kissinger	October 1982
Janine Borofka	May 1985
Theerayuth Lertsirrungsun	May 1986

#### Doctoral Degree

Robert D. Kissinger "The Densification of Nickel-Base Superalloy Powders by Hot Isostatic Pressing", anticipated January 1988

Janine C. Borofka "Kinetics and Mechanisms of Hot Isostatic Pressing of a Nickel-Base Superalloy", anticipated May 1988

#### IV. Publications and Presentations from this Research

##### Publications

- "Modeling of Hot Isostatic Pressing of Particulate Composites," J.C. Borofka and J.K. Tien (to be published).
- "Modeling of CAP<sup>TM</sup> of Superalloy Powders," R.D. Kissinger and J.K. Tien (to be published).
- "Densification of Oxide Superconductors by Hot Isostatic Pressing," J.K. Tien, J.C. Borofka, B.C. Hendrix, T. Caulfield and S.H. Reichman, submitted to Met. Trans. A.
- "Bimodal Modeling of HIP of Superalloys," J.K. Tien and J.C. Borofka, Proc. First Intl. Conf. on Hot Isostatic Pressing - Theories and Applications, Lulea, Sweden, June 1987, CENTEK Publishers, Lulea Sweden, in press.
- "P/M and ODS Superalloys and Processing," J.C. Borofka, R.D. Kissinger and J.K. Tien, chapter in Superalloys, Composites and Ceramics, eds J.K. Tien and T. Caulfield, Academic Press, Orlando FL, in press.
- "Powder Metallurgy Superalloys," J.K. Tien, J.C. Borofka and R.D. Kissinger, chapter in Rapid Solidification: Materials, Processing and Applications, ed. B. Cantor, North-Holland, Amsterdam, in press.
- "Hot Deformation Behavior of Aerospace Materials," T. Lertsirungsun, E.A. Schwarzkopf, J.C. Borofka and J.K. Tien, Proc. S.E. Asia Iron and Steel Institute Conf., Bangkok, Nov. 1986, in press.
- "Infringement of Defect Tolerant Castings on Traditional Wrought Superalloy Applications," J.K. Tien, J.C. Borofka and M.E. Casey, chapter in Advanced Materials for Severe Service Conditions, eds. K. Iida and A.J. McEvily, Proc. US-Japan Joint Seminar on Materials Needs for Severe Service Conditions, Tokyo, May 1986, Elsevier Appl. Science Publ., Essex UK, 1987, pp. 15 - 31.
- "Densification Mechanism Maps for Hot Isostatic Pressing (HIP) of Unequal Size Particles," S.V. Nair and J.K. Tien, Met. Trans. A, Vol. 18A, No. 1 (Jan. 1987) pp. 97 - 107.
- "Penetration of Precision Cast Superalloys into Wrought Superalloy Applications," J.K. Tien, J.C. Borofka and M.E. Casey, J. of Metals, Vol. 38, No. 12 (Dec. 1986) pp. 13 - 17.
- "Understanding the Kinetics and Densification Mechanisms in Hot Isostatic Pressing (HIP) of Superalloy Powders", J.C. Borofka, T. Caulfield and J.K. Tien, Metal Powder Report, Vol. 41, No. 10 (Oct. 1986) pp. 745 - 747.
- "Obtaining the Radial Distribution of Random Dense Packed Hard Spheres," S.V. Nair, B.C. Hendrix and J.K. Tien, Acta Met., Vol. 34, No. 8 (July 1986) pp. 1599 - 1605.

- "Influence of Powder Size Distribution and Pressure on Kinetics of HIP Consolidation of P/M Superalloy Rene 95," R.D. Kissinger, S.V. Nair and J.K. Tien, Superalloys 1984, eds. M. Gell et al., Proc. Fifth Intl. Conf. on Superalloys, Oct. 1984, Champion PA, TMS-AIME Press, Warrendale PA, 1984.
- "Consolidation Science of P/M Superalloys," J.K. Tien and R.D. Kissinger, Proc. 1984 Intl. P/M Conf., Toronto, June 1984, APMI, Princeton NJ, 1984.
- "Hot Isostatic Consolidation of P/M Superalloys," R.D. Kissinger, S.V. Nair and J.K. Tien, Rapidly Solidified Metastable Materials eds. B.H. Kear and B.C. Giessen, MRS Symp. Proc. Vol. 28, Elsevier Science Publ. Co. Inc., New York, 1984, pp. 157 - 162.
- "Interpretive Review of Comparative Microstructures of Powders and Consolidates of P/M Superalloys Produced by Modern Atomization Processes," R.D. Kissinger and J.K. Tien, Rapid Solidification Processing: Principles and Technologies III, ed. R. Mehrabian, Proc. Third Conf. on RSP, Gaithersburg MD, Dec. 1982, NBS, Gaithersburg MD, 1982, pp. 510 - 518.

Presentations (speaker's name underlined)

- "Near-Net-Shape Processing of Oxide Superconductors," J.K. Tien, J.C. Borofka and B.C. Hendrix, Symp. on Superconductivity and Applications, Buffalo NY, September 1987.
- "Modeling of HIP of Superalloys," J.K. Tien, J.C. Borofka and T. Caulfield, First Intl. Conf. on Hot Isostatic Pressing - Theories and Applications, Lulea Sweden, June 1987.
- "HIP of Composites", J.C. Borofka and J.K. Tien, poster session, First Intl. Conf. on Hot Isostatic Pressing - Theories and Applications, Lulea Sweden, June 1987.
- "Hot Deformation Behavior of Aerospace Materials," T. Lertsirungsun, E.A. Schwarzkopf, J.C. Borofka and J.K. Tien, Proc. S.E. Asia Iron and Steel Institute Conf., Bangkok, Nov. 1986.
- "HIP Consolidation Modeling," J.C. Borofka, S.V. Nair and J.K. Tien, TMS-AIME Fall Meeting, Orlando FL, Oct. 1986.
- "Infringement of Defect Tolerant Castings on Traditional Wrought Superalloy Applications," J.K. Tien, J.C. Borofka and M.E. Casey, US-Japan Joint Seminar on Materials Needs for Severe Service Conditions, Tokyo, May 1986.
- "Powder Metallurgy of Superalloys", J.K. Tien and J.C. Borofka, Lecture to Chinese Society of Powder Metallurgy, Taiwan, May 1986.
- "Kinetics and Mechanisms of HIP Consolidation of a Nickel-Base Superalloy," J.C. Borofka and J.K. Tien, AIME Annual Meeting, New Orleans LA, March 1986.
- "Hot Workability of Aerospace Materials," T. Lertsirungsun, J.C. Borofka, E.A. Schwarzkopf, AIME Annual Meeting, New Orleans LA, March 1986.
- "Penetration of Precision Cast Superalloys into Wrought Superalloy Applications,"

J.K. Tien, J.C. Borofka and M.E. Casey, AIME Annual Meeting, New Orleans LA, March 1986.

"Hot Workability of an as-HIP Nickel-Base Superalloy," J.C. Borofka and J.K. Tien, AIME Annual Meeting, New York, Feb. 1985.

"Influence of Powder Size Distribution and Pressure on Kinetics of HIP Consolidation of P/M Superalloy Rene 95," R.D. Kissinger, S.V. Nair and J.K. Tien, Fifth Intl. Conf. on Superalloys, Champion PA, Oct. 1984.

"Consolidation Science of P/M Superalloys," J.K. Tien and R.D. Kissinger, 1984 Intl. P/M Conf., Toronto, June 1984.

"Influence of HIP Pressure and Particle Size Distribution on Hot Isostatic Consolidation of P/M Superalloys," R.D. Kissinger, S.V. Nair and J.K. Tien, AIME Annual Meeting, Los Angeles, Feb. 1983.

"Hot Isostatic Consolidation of P/M Superalloys," R.D. Kissinger, S.V. Nair and J.K. Tien, MRS Symp., Boston, Nov. 1983.

"Interpretive Review of Comparative Microstructures of Powders and Consolidates of P/M Superalloys Produced by Modern Atomization Processes," R.D. Kissinger and J.K. Tien, Proc. Third Conf. on RSP, Gaithersburg MD, Dec. 1982.

END

FEB.

1988

DTic